Temporal Variability of Oceanic Eddy Kinetic Energy: A High Resolution Model Analysis

Master-Arbeit im

–**Masterstudiengang (M.Sc.) Climate Physics** –

Meteorology and Physical Oceanography

der Mathematisch-Naturwissenschaftlichen Fakultät

der Christian-Albrechts-Universität zu Kiel

vorgelegt von

Jan Klaus Rieck

817219

Erstgutachter: Prof. Dr. Claus Böning

Zweitgutachter: Prof. Dr. Richard Greatbatch

Kiel im Oktober 2014

Abstract

Mesoscale variability of velocities is an important part of the global ocean circulation, as it contains more kinetic energy than the mean flow over most of the ocean. Understanding its generation, dissipation and modulation processes therefore is crucial to better understand ocean circulation in general. In this thesis, a global 1/12° ocean model (ORCA12) is used to study the distribution of mean surface Eddy Kinetic Energy (EKE), its seasonal cycle and possible driving mechanisms, averaged over 26 years (1981-2007). For the calculation of EKE, the deviations from yearly mean horizontal velocities $\overline{u}, \overline{v}$ are found to be best suitable. The model is then evaluated using EKE derived from satellite altimetry (AVISO). The total EKE from the model, including ageostrophic parts, realistically reproduces the observed geostrophic mean EKE and its seasonal cycle. Seasonal cycles of surface EKE in the subtropical gyres, including most of the Western Boundary Currents (WBCs), peak in the summer months in both hemispheres. The mean EKE and amplitudes of the annual cycle are generally larger in the Pacific, compared to the Atlantic. The seasonal variations of EKE in the WBCs are driven by dissipation processes at the sea surface, namely the wind stress and thermal interactions with the atmosphere in winter. Only in the core regions of the currents other processes play a role as the surface EKE there peaks in winter/spring, not consistent with the dissipation hypothesis. The balance of dissipation and generation terms in the strong, chaotic WBCs, however, varies from year to year. In the subtropical gyres' interior, dissipation is not solely responsible for the annual cycle. Instead, the vertical shear of near-surface horizontal velocities is found to peak in summer, in phase with the EKE. This seasonal cycle of the shear can be observed down to $\sim 150m$ depth, depending on the region. Inspections of profiles of horizontal velocity and EKE reveal the vertical shear to be associated with the velocity differences between the Mixed Layer and the interior ocean, possibly leading to instabilities which locally generate surface intensified EKE, largest in summer. Therefore, the seasonal cycle of near-surface vertical shear of horizontal velocities seems to be responsible for the seasonal variations of surface EKE, although the general source of EKE in the subtropical gyres remains unclear.

Zusammenfassung

Die mesoskalige Variabilität ist ein wichtiger Teil der Ozeanzirkulation. In vielen Regionen enthält sie mehr kinetische Energie als die mittleren Strömungen. Um ein besseres Verständnis der Strömungen zu erlangen ist es daher unerlässlich die Entstehung, Vernichtung und Veränderungen der mesoskaligen Variabilität zu verstehen. In dieser Arbeit wird ein globales 1/12° Ozeanmodell (ORCA12) benutzt um die räumliche Verteilung der über 26 Jahre (1981-2007) gemittelten, oberflächennahen kinetischen Wirbelenergie (EKE), ihren Jahresgang und mögliche Ursachen zu untersuchen. Zur Berechnung der EKE eignen sich Abweichungen von jährlich gemittelten Geschwindigkeiten $\overline{u}, \overline{v}$ am Besten. Mit Hilfe von EKE aus Satellitenaltimetrie (AVISO) wird dann die Leistung des Modells getestet. Die EKE, inklusive ageostrophischer Anteile, aus dem Modell kann die EKE und ihren Jahresgang der beobachteten geostrophischen EKE realistisch widergeben. Die Jahresgänge der EKE in den subtropischen Wirbeln und großen Teilen der westlichen Randströme (WBCs) haben ihr Maximum im Sommer. Die mittlere EKE und die Amplituden der Jahresgänge im Pazifik sind größer als die im Atlantik. Die saisonalen Veränderungen der EKE in den WBCs, mit Ausnahme der Kernregionen, wird durch Vernichtungsprozesse an der Meeresoberfläche verursacht; zu nennen sind hier die Windschubspannung und thermische Wechselwirkungen mit der Atmosphäre im Winter. Die Balance zwischen Vernichtung und Entstehung in den intensiven WBCs variiert aber stark von Jahr zu Jahr. Im Inneren der subtropischen Wirbel sind die Vernichtungsprozesse nicht alleinig verantwortlich für den beobachteten Jahresgang. Stattdessen zeigt die mittlere vertikale Scherung der horizontalen Geschwindigkeiten der oberen $\sim 150m$, je nach Region, ein deutliches Maximum im Sommer, analog zur EKE. Vertikale Profile der horizontalen Geschwindigkeiten und der EKE zeigen eine vertikale Scherung im Zusammenhang mit Geschwindigkeitsunterschieden zwischen der Deckschicht und dem tieferen Ozean. Diese Scherung kann möglicherweise zu Instabilitäten führen, die lokal oberflächenintensivierte EKE generieren, besonders im Sommer. Daher ist es wahrscheinlich, dass dieser Jahresgang der oberflächennahen Scherung für die saisonalen Schwankungen der EKE an der Oberfläche verantwortlich ist. Eine allgemeine Quelle der EKE in den subtropischen Wirbeln kann hiermit allerdings nicht nachgewiesen werden.

Contents

1 Introduction

1.1 Observations of Eddy Kinetic Energy

In the early stages of physical oceanography, the currents in the ocean were mostly described as a slow, laminar flow. Due to very sparse data in time and space, no more precise representation could be achieved than this highly smeared, rather schematic one. Up until the 1970s, apart from observations of meanders and large eddies associated with the strongest currents, only suggestions about the existence of mesoscale variability could be made (Robinson, 1983). C. O'D. Iselin was the first to identify a strong eddy north of the Gulf Stream in the 1930s (Iselin, 1936), when he evaluated temperature and salinity measurements in order to derive the density of the water and associated relative geostrophic currents. More and more evidence of a highly variable, narrow and meandering Gulf Stream and also a deep countercurrent in the North Atlantic was found during multiple surveys in the 1950s (Swallow, 1976). It was not until the 1970s though, that the idea of eddies being present in all regions of the oceans became widely accepted.

Accompanying the advance of measurement techniques, an inhomogeneous distribution of Eddy Kinetic Energy (EKE) in the world's oceans was found. Wyrtki et al. (1976) and Dantzler (1977) derived a basin-wide picture of mesoscale variability using ship drift and XBT (Expendable Bathythermograph) data, respectively. One milestone of the detection of highly energetic regions in the mesoscale was the 1970s Mid-Ocean Dynamics Experiment (MODE) which clearly pointed out the Western Boundary Currents (WBCs) as a source for local and remote EKE (MODE Group, 1978). The mesoscale variability was defined to be in the order of tens to hundreds of kilometers on the spatial scale and weeks to months on the temporal (Stammer and Böning, 1996). The kinetic energy at these scales was found to be stronger than the Mean Kinetic Energy (MKE, the kinetic energy of the mean flow) by an order of magnitude or more (Xu et al., 2011). Various forms of mesoscale variability have been studied: Meandering and filamenting of strong currents that occasionally lead to partial or total shedding of ring currents, planetary and topographic waves, different forms of vortices (surface- or depth-intensified, barotropic) etc. (Robinson, 1983). The importance of eddies for heat and momentum

fluxes and their impact on the whole climate system has then also been acknowledged.

The wide use of satellite altimetry data of the Sea Surface Height (SSH) and associated geostrophic currents was a further major improvement to the understanding of the surface EKE distribution in the world's oceans. Particularly the parts with a lower variability level could then be better resolved. For the first time basin-wide, synoptic maps with a high temporal resolution were created with the Seasat altimetry mission (Fu, 1983), even though it only operated for little more than three months. Today, much longer timeseries are available with the ERS-1 and -2 missions having a combined operating time from 1991 to 2011 and TOPEX/Poseidon operating from 1992 to 2006. First global statistics of mesoscale variability were calculated from these missions in the early nineties (Le Traon and Morrow, 2001) but a high spatial resolution with low background noise level was not achieved until TOPEX/Poseidon and ERS-1/-2 data were combined (Ducet et al., 2000). This combination showed more accurate maxima and many details in the low energy regimes. Jason-1 (2001-2013) and Envisat (2002-2012) data are also available and one of the advantages of at least two satellites being spaceborne simultaneously is the possibility of combining the resulting altimetry data. Nowadays, high resolution altimetry data from 1992 on are available without gaps and with low noise level. Currently Jason-2 (since 2008) and Cryosat-2 (since 2010) are in orbit (AVISO, 2014). The mean surface EKE derived by satellite altimetry shows maxima of over $4500 cm^2 s^{-2}$, whereas about 70% of the oceans have a mean EKE of less than $300 cm^2 s^{-2}$ (Scharffenberg and Stammer, 2010; Xu et al., 2011). The regions with highest mesoscale variability are the WBCs, especially the Gulf Stream (GS) and Kuroshio/Oyashio Extension systems, and the Agulhas Retroflection, with EKE values higher than $2000 cm^2 s^{-2}$. Also notable are the Northwest Indian Ocean (Great Whirl) and the Gulf of Mexico with EKE $> 1000 cm^2 s^{-2}$ as well as the Antarctic Circumpolar Current (ACC) and the equatorial regions of all oceans with EKE above $300 cm^2 s^{-2}$. The remaining parts of the oceans show EKE $< 300 cm^2 s^{-2}$ with minima in the polar oceans and the interior South Atlantic and North Pacific (EKE $< 30 cm^2 s^{-2}$).

1.2 Eddy Kinetic Energy in Numerical Models

Simultaneously to the systematic observations of oceanic variability in the 1970s, first attempts of assessing the role of eddies in the ocean with numerical models were made. The developed models had a resolution of less than $100km$ in the horizontal. Although these studies were carried out in idealized basins, mostly located in the mid-latitudes, first promising results could be obtained (Holland et al., 1983). The strong jets and currents in these simulations produced baroclinic and barotropic instabilities, generating an eddy field which also radiated energy into more distant regions of the basins (Holland and Lin, 1975; Robinson et al., 1977). With grid resolutions in the order of a few tens of kilometers and eddy sizes of a few hundred kilometers in the modelled regions, the full cycle from eddy generation to dissipation could be simulated. Starting with the potential energy of the mean flow feeding energy into the mesoscale, to the dissipation of this energy, mostly by bottom friction (Semtner and Mintz, 1977). In the 1980s, Cox (1985) first integrated an eddy-resolving numerical model for a realistically dimensioned ocean basin. Although this basin was still idealised, it was a major contribution to the simulation of eddy-resolving wind- and thermohaline-driven numerical models. The deficiencies of this and other models of that time were then met in the 1990s with models of increasing resolution and more realistic topography and horizontal boundaries (Stammer and Böning, 1996). In the late 1990s and early 2000s, global numerical ocean models with 40-50 vertical levels and 8-10km horizontal resolution were in wide use. Smith et al. (2000), for the first time reported an accurate agreement of simulated and observed EKE from satellite altimetry in their Parallel Ocean Program (POP) 1/10° ocean general circulation model. Apart from the increasing resolution many other features have been improved. The numerical implementation, parametrization of the sub-grid scale processes as well as the surface forcing and topography products being some of them (Maltrud and McClean, 2005).

1.3 Sources, Sinks and Variability of Eddy Kinetic Energy

With a constantly improving view of the global ocean's EKE developing, the question of generation and dissipation processes arose. In general, oceanic variability can be seen

as a direct or indirect response to local or remote atmospheric forcing (Stammer and Wunsch, 1999). The direct response manifests itself in variability caused by wind stress and buoyancy forcing, while there are different mechanisms for the indirect response. Gradients in current velocities lead to dynamically unstable processes depending on the strength of the gradient. The flow of currents over topographic features and meandering of strong currents are other major sources for mesoscale variability in the ocean. Even though it is not a difficult task to generally point out the sources for EKE in the ocean, up to date there is no reliable theory of local eddy energy generation and dissipation (Xu et al., 2011). In the WBCs and other strong currents, the local maxima in EKE can be easily explained by the meandering and sharp gradients in velocity, thus high baroclinic and barotropic instability. The interior of the mid-latitude oceans, however, does not show these instability processes on a large scale, nevertheless eddy energy in the mesoscale is present. Different possibilities concerning the sources for this variability have been investigated. The first theory focusses on baroclinic instability, which is clearly the source in western boundary currents. The energy generated in these currents was believed to radiate towards the ocean's interior. This theory, however, has been proven to be insufficient to explain the observed spectrum of EKE in these remote regions (Stammer et al., 2001). The second theory proposes the EKE in the mid-oceans to be generated locally by fluctuating winds. It was shown though, that eddy energy generated directly by wind stress is the source for barotropic currents and Rossby waves and cannot explain the full spectrum of energy found. Nevertheless, direct mechanical forcing from the atmosphere is mostly responsible for EKE in the deep ocean (Willebrand et al., 1980; Fukumori et al., 1998). The contribution of direct wind forcing to the local surface EKE fields seems to be of minor importance, except for in a few regions with very low energy levels (Stammer, 1997).

One way to attribute some sources to the EKE observed in the ocean, is the study of its temporal variability. A seasonal cycle or interannual changes in the source of EKE (be it baroclinic instability/current velocity or atmospheric forcing like wind) should manifest themselves in a seasonal cycle or interannual changes in the observed EKE. The first study to point out a seasonality in EKE was by Dickson et al. (1982), who found

a winter maximum of near-surface EKE at various sites in the eastern North Atlantic. Varying wind stress was suggested as a source. Using satellite altimetry, Stammer and Wunsch (1999) mapped the seasonal cycle of surface EKE (its amplitude and phase) for the whole globe. They found widely distributed winter and spring maxima in the eastern North Atlantic and Pacific and along the North Equatorial Currents, while the western subtropical gyres and North Equatorial Counter Currents (NECC) show maxima in EKE in summer and fall. Investigations of interannual changes in surface EKE are much more limited due to the lack of long-term observations with the required spatial coverage and the computational effort of long model runs with the necessary resolution of the grid. In most cases, interannual changes in observed surface EKE are associated with shifting positions of the currents that generate the EKE through instabilities (Hakinen and Rhines, 2009; White and Heywood, 1995; Volkov, 2005). Brachet et al. (2004) find interannual changes of EKE derived from satellite altimetry to be often associated with drifts in wind stress fields but Stammer and Wunsch (1999) point out that EKE from moorings generally shows no significant interannual variations. Thus, an investigation of the seasonal cycle of surface EKE appears more promising to deliver significant results.

The aim of this study is to evaluate the seasonal cycle of surface EKE in greater detail using a global ocean general circulation model. The model's performance in simulating EKE at a global and regional level is tested against observational EKE from satellite altimetry. Furthermore, the seasonal cycle of EKE is investigated and several mechanisms possibly responsible for the variability on a seasonal scale are tested in a few selected regions of the world oceans. The regions are chosen based on model data that is validated with satellite altimetry. The six regions are: The Gulf Stream and Kuroshio regions, adjacent regions in the western northern hemisphere subtropical gyres and their southern hemisphere counterparts.

The Gulf Stream System (GS) has been studied most extensively of all current systems and therefore provides a good comparison to other studies. One of the first investigations of the near-surface EKE in the GS was carried out by Richardson (1983) with satellite-tracked drifting buoys. He found a maximum mean EKE levels of around

$3000cm^2s^{-2}$ but no evidence of a seasonal cycle. Maximum mean surface EKE values in the range $3000cm^2s^{-2}$ to $5000cm^2s^{-2}$ have been confirmed by later model (Smith et al., 2000) and altimetry studies (Stammer and Wunsch, 1999; Brachet et al., 2004), who also found a seasonal signal with minimum values in winter and a maximum in late summer/early fall (August/September). Ducet and Le Traon (2001) and Zhai et al. (2008), also using satellite altimetry, found the maximum of the seasonal cycle to be in July. Zhai et al. (2008) found the summer surface EKE to be higher than winter values in most of the North Atlantic, up to 30% in the GS region, and propose an annual minimum in the eddy dissipation rate to be responsible. The distribution of surface EKE could also be reconstructed using high-resolution numerical models. Smith et al. (2000) used a $1/10°$ model of the North Atlantic and got accurate EKE values but did not investigate any temporal variability of EKE. It has also been shown that the seasonal cycle of surface EKE in the GS exhibits strong interannual changes. Volkov (2005) states that these changes are preceded by two years by extreme events of the North Atlantic Oscillation (NAO).

The Kuroshio/Kuroshio Extension System is comparable to the GS in dynamics and is thought to show similar characteristics of flow and EKE. A number of studies based on satellite altimetry exist which agree upon maximum surface EKE values between $2000cm^2s^{-2}$ and $5000cm^2s^{-2}$ with maximum values in the western part and decreasing EKE towards the east. The maximal eastward extend of high energy levels vary from $158°E$ (Ducet and Le Traon, 2001) to $175°W$ (Qiu, 2002). The maximum of the seasonal cycle varies from May/June close to Japan's coast and July/August in the Kuroshio Extension (Adamec, 1998; Ducet and Le Traon, 2001; Stammer and Wunsch, 1999), being highly variable in between different years. As for the GS, regional model studies succeed in reproducing the mean EKE distribution (Hurlburt et al., 1996) but few investigations have been carried out concerning the temporal variability, seasonal signals in particular.

In addition to these WBC regimes, the adjacent regions in the interior of the subtropical gyres will be studied. The EKE in these regions is generally low, in the order of $50cm^2s^{-2}$ to $300cm^2s^{-2}$ in the North Atlantic (NA) and North Pacific (NP), and even lower in the southern hemisphere (SH) counterparts (Scharffenberg and Stammer,

2010). Nevertheless, the interannual variability is not as large as in the highly energetic regions and thus the probability to find a robust seasonal cycle is most likely higher. Scharffenberg and Stammer (2010) and Zhai et al. (2008) found seasonal cycles with maxima in the summer months in the subtropical regions adjacent to the WBCs in the western NP and western NA.

For further comparison, especially regarding the identification of possible mechanisms, similar regions in the SH will be studied as well. Especially in the subtropical gyres, an investigation of the seasonal cycle and its sources is thought to also shed some light onto the question of the source of EKE in these regions in general, which remains highly debated to date (Xu et al., 2011).

Following this introduction, the data and model output are introduced in section 2. The applied methods are described and discussed in section 3, with a special focus on the calculation of EKE in section 3.2. In section 4 the results are presented, starting with the assessment of the ORCA12 model on a global scale in section 4.1, followed by detailed investigations of the mean EKE and seasonal variations of the WBCs and subtropical gyres in sections 4.2 and 4.3, respectively. The discussion of possible mechanisms for the observed seasonal cycle is placed in section 5, followed by a summary and conclusion in section 6.

2 Data and Model Output

2.1 AVISO

The observational Sea Surface Height (SSH) data used in this study was obtained by satellite altimetry and distributed by "Archiving, Validation and Interpretation of Satellite Oceanographic Data" (AVISO). The data used is extracted from the "dataset-duacs-dt-upd-global-merged-madt-h-daily" dataset found on "http://opendap.aviso.oceanobs.com/thredds/dodsC/" and produced by SSALTO/DUACS (SSALTO/DUACS, 2014) with the help of the Centre National d'Etudes Spatiales (CNES). The dataset is a combination of altimetry measurements from various satellites (TOPEX/ Poseidon, Jason-1, ERS-1/2, Envisat) which use radar technique on different wavelengths to calculate the

distance between each satellite and the sea surface by measuring the time it takes an electromagnetic wave to travel from the satellite to the sea surface and back.

Several corrections have to be made to the travel times. First of all, the orbit of the satellite has to be determined. This is achieved by GPS measurements in combination with a "Precise Orbit Ephemeris" (POE). This ephemeris is a table with accurate positions of astronomical bodies and also of satellites. The travel time of the electromagnetic waves has to be corrected for the interaction with electrons in the ionosphere as well as dry gases, water vapour and water in the lower atmospheric layers. After taking into account the influence of and the interaction with the atmosphere, there are still corrections to be made concerning the influence of various tides and atmospheric pressure on the SSH. The undulations of the oceans, but also the solid earth, through the gravitational attraction of the sun and the moon are the most important tides. But also changes of SSH due to variations of the rotational axis of the earth have to be considered. Furthermore the reflectivity of the sea surface changes with different wave heights.

After completing the numerous corrections and undergoing a quality control procedure, the altimetry data is calibrated at crossing points of the different satellites tracks and SSH is determined in relation to a reference height. To get an absolute SSH, a mean dynamic topography is added. This mean dynamic topography is based on four and a half years of gravimetric data from the Gravity Recovery and Climate Experiment (GRACE) as well as 15 years of satellite altimetry and in-situ measurements from e.g. drifting buoys. After this calibration the SSH data is interpolated onto a $1/4^\circ \times 1/4^\circ$ grid with a temporal resolution of one day. This study uses data spanning a time period from 01. January 1993 to 31. December 2007. For EKE calculations geostrophic horizontal velocities u and v are used that are also distributed by AVISO. Near the equator, an equatorial geostrophy approach to derive velocities from SSH is used by AVISO. As the equatorial regions are not of any interest to this study this method is not described in more detail and equatorial regions will be masked in global maps because the geostrophic EKE of AVISO and the EKE of ORCA12 including the ageostrophic part cannot be compared at the equator (cf. Fig. 3).

More information on AVISO SSH data and associated errors are found in Ducet

et al. (2000), Le Traon et al. (1998) and SSALTO/DUACS (2011). For a general description of satellite altimetry and its performance in measuring the mesoscale variability in the ocean see Le Traon and Morrow (2001).

2.2 ORCA12

The simulated data in this study are taken from the ORCA12 model configuration. ORCA12 is based on the NEMO (Nucleus for European Modelling of the Ocean) code (Madec, 2008). NEMO is a framework for various ocean models. The two important models for this study are the engine for ocean dynamics and thermodynamics Océan PArallélisé (OPA) (Madec et al., 1998) and the engine for sea-ice dynamics and thermodynamics Louvain-la-neuve Ice Model (LIM2) (Fichefet and Morales Maqueda, 1997). OPA version 8 is the base for the ocean component of the NEMO code. The ORCA12 configuration uses a global, orthogonal, curvilinear, tripolar grid to avoid singularities at the North Pole (Scheinert, 2014). The grid is a staggered Arakawa-C type grid; the tracer points are located in the middle of each grid box while the velocity points U,V and W are shifted eastward, northward and upward to the boundary of the grid cell, respectively. In ORCA12 this grid has a nominal resolution of $1/12^\circ$ in the horizontal which is below the internal Rossby radius of deformation at the latitudes investigated in this study. Therefore, it is able to represent the mesoscale variability. In the vertical there are 46 levels with $6m$ layer thickness at the surface and about $250m$ in the deep ocean. Partial bottom cells and advanced advection schemes are used (Barnier et al., 2006).

The model run used in this study is ORCA12.L46-K001. It uses partial slip boundary conditions (Scheinert et al., 2014) and an atmospheric forcing as described in Large and Yeager (2004) and proposed by the Coordinated Ocean-Ice Reference Experiments (CORE, Griffies et al. (2008)). The horizontal mixing coefficients, namely tracer diffusivity A_h^t and momentum viscosity A_h^m, are dependent on the horizontal grid scale. $A_{h0}^t = 125m^2s^{-1}$, $A_{h0}^m = 1.25 \times 10^{10}m^4s^{-2}$ are highest at the equator, decreasing towards the poles. Vertical tracer diffusivity and momentum viscosity are implemented through a Turbulent Kinetic Energy (TKE) model (Blanke and Delecluse, 1993; Gas-

par et al., 1990) which modifies the background mixing coefficients $A^t_{v0} = 1.2 \times 10^{-5}$ and $A^m_{v0} = 1.2 \times 10^{-4} m^2 s^{-1}$. The TKE model does not penetrate below the Mixed Layer. Five day mean zonal and meridional surface velocities from 01 Jan. 1981 to 31. Dec. 2007 are used in this study for the calculation of EKE. For further investigation, monthly means of wind stress τ, temperature and salinity (to derive potential density) and velocities (to derive vertical shear) are used from the model output.

For investigations of EKE at $100m$ depth, a second model run (ORCA12.L46-K004) was used due the lack of available data at this depth from the first run. K004 differs from K001 in some boundary conditions, e.g. a free-slip boundary condition, and some salinity restoring terms but the distribution of EKE is not affected significantly in the regions investigated here. The findings from the K004 run are therefore assumed to be transferable to the main model run K001 (Fig. 2).

3 Methods

3.1 Sea Surface Height Variance

To calculate the Sea Surface Height variance, a global trend is removed from every time series on the grid points. For every five day period a global mean sea level is calculated to get the global trend over the whole time from 1 Jan. 1993 to 31 Dec. 2007 for AVISO and 1 Jan. 1981 to 31 Dec. 2007 for ORCA12. This global trend is then subtracted from every single time series. After removing the trend the SSH variance is caculated at every grid point with respect to the 15-year mean.

$$\sigma^2_{SSH} = \frac{1}{n} \sum_{i=1}^{n} (SSH_i - \overline{SSH})^2 \tag{1}$$

where n denotes the number of five-daily SSH values. The procedure is the same for the AVISO and ORCA12 data. For the AVISO data however, the daily interpolated values are averaged over five day periods to be comparable to the model output.

3.2 Eddy Kinetic Energy

The Eddy Kinetic Energy for the ORCA12 model output is calculated directly from the meridional and zonal velocity outputs u and v. To be comparable to the AVISO altimetry data, the geostrophic velocities have to be derived from gradients of SSH as follows:

$$u_{geo} = -(\frac{g}{f})\frac{\partial SSH}{\partial y} \tag{2}$$

$$v_{geo} = (\frac{g}{f})\frac{\partial SSH}{\partial x} \tag{3}$$

where g is the gravitational acceleration $g \approx 9.8 m^2 s^{-2}$, varying with latitude, and φ is the latitude. $f = 2\Omega \sin(\varphi)$ is the Coriolis parameter with $2\Omega = 1.458 \times 10^{-4} s^{-1}$, twice the rotation rate of the earth.

To calculate EKE (equation (4)), first the mean zonal and meridional surface velocities, $\overline{u}$ and $\overline{v}$, respectively, are derived on a global scale. The period over which the time mean is taken to derive anomalies is quite an interesting matter. Depending on which processes and time scales are to be considered, different reference periods can be chosen. Most studies choose to calculate EKE from anomalies u' and v' with respect to a multi-year averaged $\overline{u}$ and $\overline{v}$. Problems arising using this method can be seen in figure 1. Interannual variations of the mean velocities are regarded as anomalies contributing to the EKE (cf. Penduff et al. (2004)), although, by definition, the EKE is the mesoscale variability of kinetic energy with time scales of weeks to months (Stammer and Böning, 1996). This insufficiency can be overcome by taking annual mean $\overline{u}$ and $\overline{v}$ as reference velocities. This leads to substantial differences of up to $400 cm^2 s^{-2}$, for example in the GS region. The interannual variations in this region are not observed to be subject to substantial change though. This may be due to the fact that, especially in regions with strong mean currents, the EKE resulting from instabilities in the current is closely connected to the actual strength and velocity of the mean current.

Considering shorter time scales such as the annual cycle of EKE, the possible annual cycle of the mean velocities $\overline{u}$ and $\overline{v}$ should be taken into account. There are several ways this could be done. First, a mean annual cycle of u and v could be subtracted before

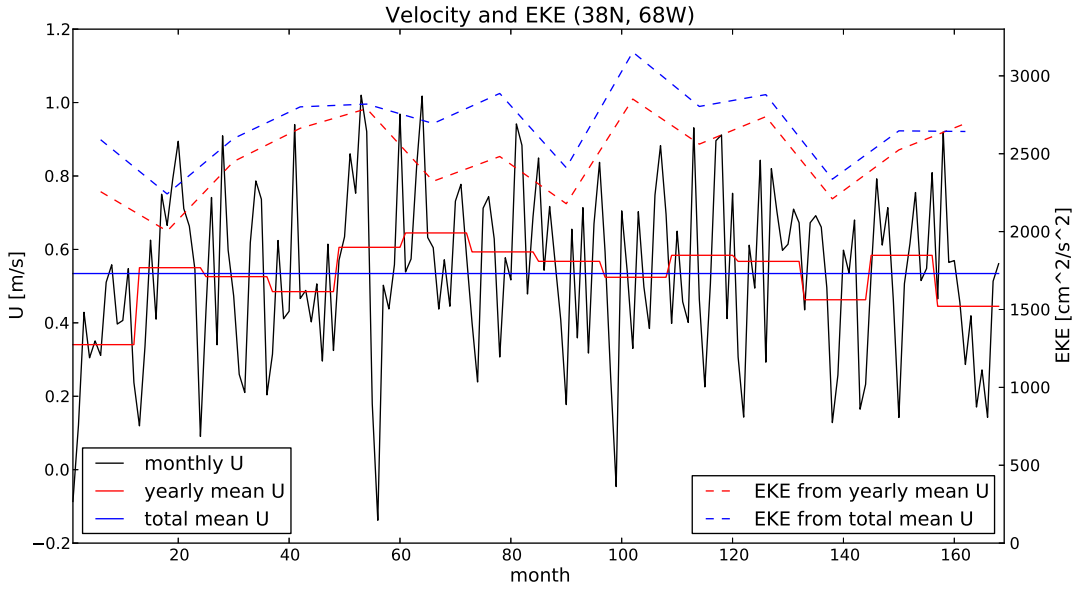

Figure 1: Comparison of EKE calculated from deviations from yearly mean velocities (red lines; solid: mean velocity U; dashed: EKE) and total mean (168 months) velocities (blue lines). The black solid line shows the monthly mean U.

calculating EKE and second, the EKE could be calculated with respect to a seasonal (three month) mean of u and v. Regarding the second method, care has to be taken as large features of mesoscale variability might have time scales of a couple of months and calculating EKE to a seasonal mean velocity could neglect a part of that variability. However, the seasonal cycle of the mean flow in the midlatitudes only affects the calculated EKE in its mean, not in the amplitude and phase of its seasonal cycle (Fig. 2). Therefore, in this study a yearly mean $\overline{u}$ and $\overline{v}$ and its deviations u' and v' are used to calculate the EKE:

$$EKE = \frac{1}{2}(u'^2 + v'^2) \tag{4}$$

where $u' = u - \overline{u}$; $v' = v - \overline{v}$. This gives qualitatively similar results to the calculations considering a seasonal mean and has the benefit of not neglecting any mesoscale variability of relatively long time scales.

To derive the mean seasonal cycle of EKE for every grid point, all five day average values that have the center of their time span in one specific month are averaged and then, the months from all years are averaged. For example, for every year, all five day mean EKE values centered in January (a five day mean from 29 Jan. to 2 Feb. will be

considered as a January value as the center of the time span is 31 Jan.) are averaged. Then the Januaries from all available years are averaged.

$$EKE(i) = (\sum_{j=1981}^{j=2007} \overline{EKE_j(i)})/26 \qquad ; i = 1, ..., 12 \tag{5}$$

where i represents the months from January to December and $\overline{EKE_j(i)}$ is the mean EKE of month i in year j.

A seasonal cycle in the form of

$$A\sin(\frac{t}{12}) + B\cos(\frac{t}{12}) + C \qquad ; t = 1, ..., 12 \tag{6}$$

is then fitted to the monthly climatological values of EKE in order to focus on the seasonal cycle only and not on variability on shorter timescales, e.g. semi-annual cycles. It can be shown (Appendix II) that this fitted function in fact is a sine:

$$D\sin(\frac{t}{12} + \phi) + C \tag{7}$$

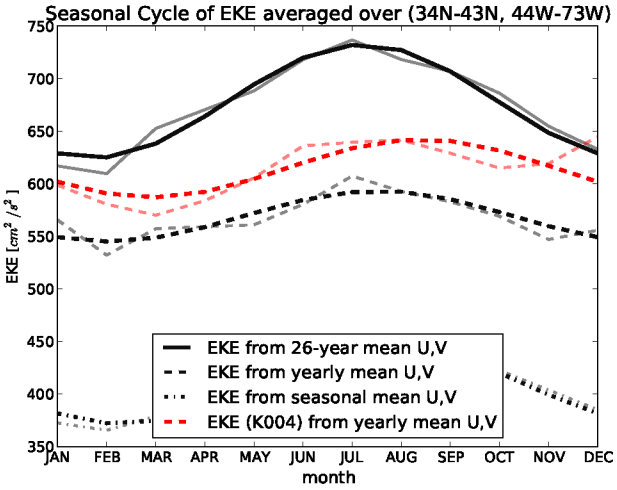

Figure 2: Comparison of the seasonal cycle of EKE calculated from deviations from total (26 years) mean velocities (solid), annual mean velocities (dashed) and seasonal (3 months) mean velocities (dash-dotted) for the Gulf Stream region. The red lines indicate the seasonal cycle of surface EKE taken from the second model run (ORCA12.L46-K004).

where $D = \sqrt{(A^2 + B^2)}$ is the amplitude, $\phi = \arctan(\frac{B}{A})$ is the phase and C is the mean value. The amplitude of the seasonal cycle is then defined to be $AMP_{EKE} = 2D$, which is the difference between the maximum and the minimum in the seasonal cycle. The phase of the seasonal cycle is defined to be the month with the maximum EKE $\phi_{EKE} = \phi + \frac{\pi}{2}$. Note that ϕ denotes the shift of the zero-crossing, if $\phi = 0$, the zero-crossing, and not the maximum, is at $t = 0$.

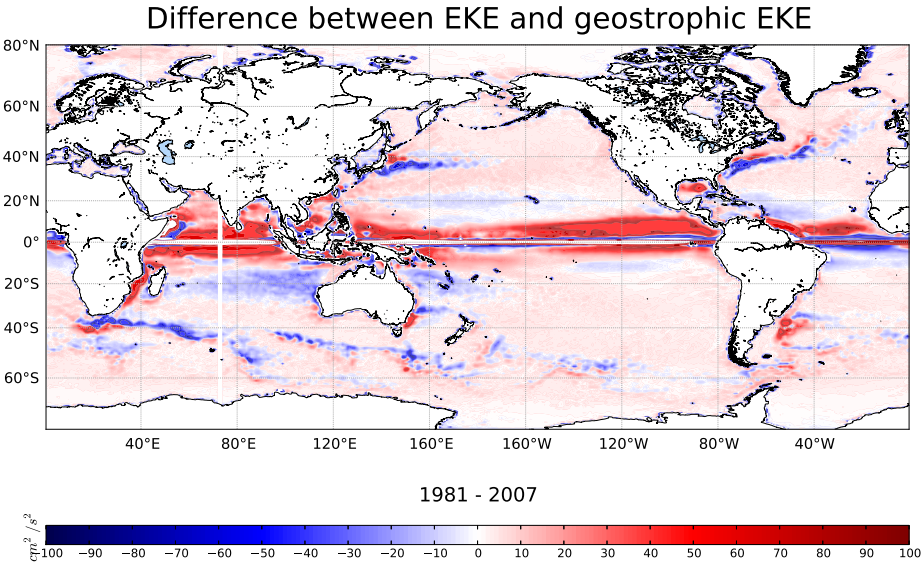

Figure 3: Difference between EKE and only geostrophic EKE in ORCA12, units: $cm^2 s^{-2}$.

For the regionally averaged seasonal cycles, first the monthly EKE is spatially averaged over the region of interest. Then all values belonging to the same months are averaged to get the seasonal cycle.

$$EKE_i^{reg} = (\sum_{x=x_1^{reg}}^{x_2^{reg}} \sum_{y=y_1^{reg}}^{y_2^{reg}} EKE_i(x,y))/((x_2^{reg} - x_1^{reg})(y_2^{reg} - y_1^{reg})) \tag{8}$$

where x_1^{reg} and x_2^{reg} are the zonal and y_1^{reg} and y_2^{reg} the meridional limits of the region of interest. For the interannual variability of EKE all values of one specific year are averaged, resulting in a timeseries of EKE with yearly values.

Another crucial point to check, is the fact that modelled EKE will be compared to EKE calculated from satellite altimetry SSH. While the AVISO based EKE only contains mesoscale variability of the geostrophic velocities, the EKE from ORCA12 is based on surface velocities that also contain ageostrophic components of the flow, such as inertial and Ekman currents. To avoid this problem, most model-based studies of mesoscale variability use velocity data from sub-surface regions (Stammer et al. (2001) use velocities from $91m$ depth for example) or calculate geostrophic currents from modelled SSH (Brachet et al., 2004). However, in this study the total surface currents u and v are

used, including the ageostrophic parts. Regarding the investigation of the seasonal cycle of EKE and especially its causes this is probably an important issue, as many of the proposed mechanisms and theories concerning the production and dissipation of EKE are connected to the atmosphere (windwork and thermal capping for example). Hence, the surface layer plays a crucial role.

In ORCA12, the ageostrophic part of the EKE is about $10cm^2s^{-2}$ in major parts of the world's oceans (Fig. 3, geostrophic EKE is $\sim 10cm^2s^{-2}$ smaller than total EKE). In some key regions though, there are significant differences. First, in all subtropical ocean basins the geostrophic EKE (EKE_{geo}) is actually $\sim 10cm^2s^{-2}$ larger than the total EKE near the tropics and second, all strong current systems (GS, Kuroshio, Agulhas Return Current, ACC) show EKE_{geo} that is up to $100cm^2s^{-2}$ smaller at the poleward side of the current and $100cm^2s^{-2}$ larger at the equatorward side. The reasons for this were not investigated but an influence of inertial currents in the Mixed Layer on eddies in these regions could play a role. Near the equator, the ageostrophic part of EKE is also considerably large due to the limits imposed on geostrophic current calculation there.

Though there are substantial differences in the mean EKE_{geo} and total EKE, the

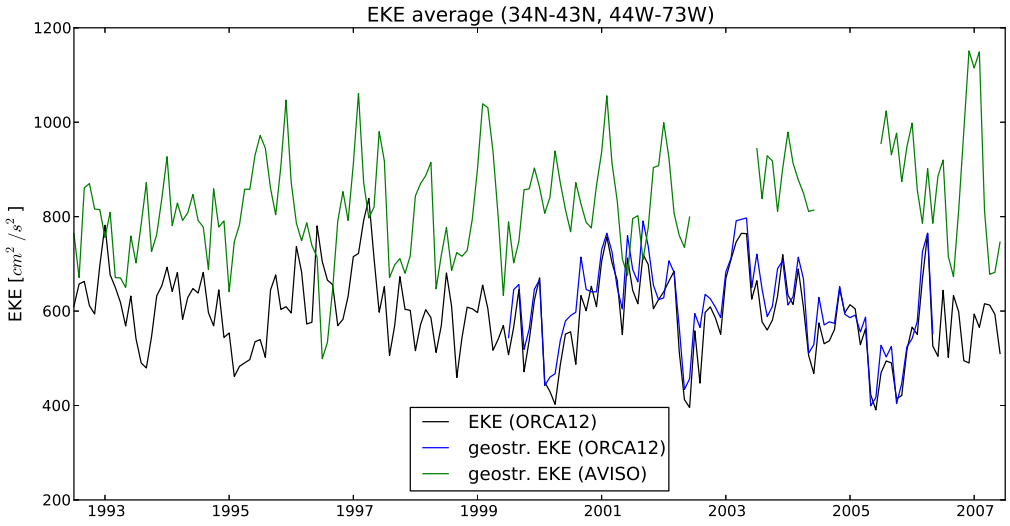

Figure 4: Timeseries from Jan 1993 - Dec 2007 of monthly EKE averaged over the Gulf Stream region (34N-43N, 44W-73W). Shown are the total ORCA12 EKE including ageostrophic part (black), geostrophic ORCA12 EKE (blue) and geostrophic AVISO EKE (green), units: cm^2s^{-2}.

temporal variability is not influenced. In figure 4 the time series of EKE in the GS is shown, a region with large differences between EKE_{geo} and total EKE in the mean. Nevertheless, the interannual and monthly variations of EKE_{geo} at this location follow the variations of total EKE remarkably well.

4 Model Assessment and Results

The first step of this study is to validate the model output with satellite altimetry. Furthermore, regions in the world's oceans with a relatively high eddy activity and homogeneous spatial distribution of the phase of the seasonal cycle have to be identified. With this selection of regions the consideration of only significant seasonal cycles can be assured. To accomplish these tasks, global maps of SSH variance and EKE are evaluated in section 4.1 before specific regions will be investigated in sections 4.2 and 4.3.

4.1 Global

4.1.1 Sea Surface Height Variance

One of the easiest and fastest ways to test oceanic variability is to inspect the variance of SSH. On a global scale, the AVISO SSH variance is highest in regions of strong currents, as expected (Fig. 5). Maximal values between $0.1m^2$ and $0.5m^2$ are reached in the Gulf Stream/North Atlantic Current (NAC) and Kuroshio/Oyashio systems and in the Gulf of Mexiko in the northern hemisphere (NH). In the southern hemisphere (SH) such high SSH variance is found in the Agulhas retroflection and the Agulhas Return Current as well as the East Autralian Current (EAC) and in the Brazil-Malvinas Confluence Zone. Much of the Antarctic Circumpolar Current (ACC), Indian Ocean and Western and Equatorial Pacific show a variance between $0.5 \times 10^{-3}m^2$ and $0.5 \times 10^{-2}m^2$ while the interior of North and South Atlantic and Pacific and also the polar oceans of both hemispheres show low SSH variances of the order $1 \times 10^{-3}m^2$ with minima found in the subtropical South Atlantic (SA) and close to the Antarctic continent. Compared to previous studies of global SSH variability, these results are similar (compare Ducet et al. (2000) Fig. 4 to Fig. 5 and 6 of this study, note that Ducet et al. (2000) show the square root of the

variance and units are cm while in this study units are m^2).

In ORCA12, the spatial pattern of SSH variance is in general agreement with the AVISO data (Fig. 6), although the extrema are not as pronounced. While wide parts of the Indian and Pacific Oceans exhibit a variance of $0.5 \times 10^{-3} m^2$ to $0.5 \times 10^{-2} m^2$ and are very similar in AVISO and ORCA12, the maxima in WBCs are lower in ORCA12, reaching only $0.2 m^2$ to $0.3 m^2$. Also the minima are not as extreme in ORCA12 with lowest values in the order $0.3 \times 10^{-3} m^2$, except for the SA.

The largest disagreement is found in the subpolar and polar oceans of the SH, south of the ACC, where SSH variance in ORCA12 is about 10 times higher than in AVISO on a large scale. With a horizontal resolution of $1/3° \times 1/3°$, the AVISO grid is very likely to be too coarse to resolve great parts of the mesoscale activity in the polar oceans. As this region is not of any interest to this study though, this major difference is not being investigated any closer.

Especially compared to previous global model studies of oceanic variability, the realism of ORCA12 has to be emphasized. In contrast to Maltrud and McClean (2005) for example, ORCA12 performs very well in regions like the Northwest Corner of the NAC, the Agulhas Return Current and the pathway of the Agulhas Rings into the SA as well as the eastern North Pacific and the Brazil-Malvinas-Confluence Zone in reproducing the SSH variance observed by satellites.

4.1.2 Mean Eddy Kinetic Energy

The global distribution of mean surface EKE from AVISO (Fig. 7) resembles that of the SSH variance, as the EKE is also closely connected to the strong current systems and the associated instabilities. Maxima $> 3000 cm^2 s^{-2}$ are found along the GS, the Kuroshio and the Agulhas Retroflection. Elevated EKE levels of $\sim 1000 cm^2 s^{-2}$ exist in various regions along the ACC, in the SH WBCs, such as the EAC, the NAC and along the equator in all ocean basins, especially pronounced along the North Equatorial Counter Current in the North Atlantic (NA). Regarding the geostrophic EKE near the equator, the inability

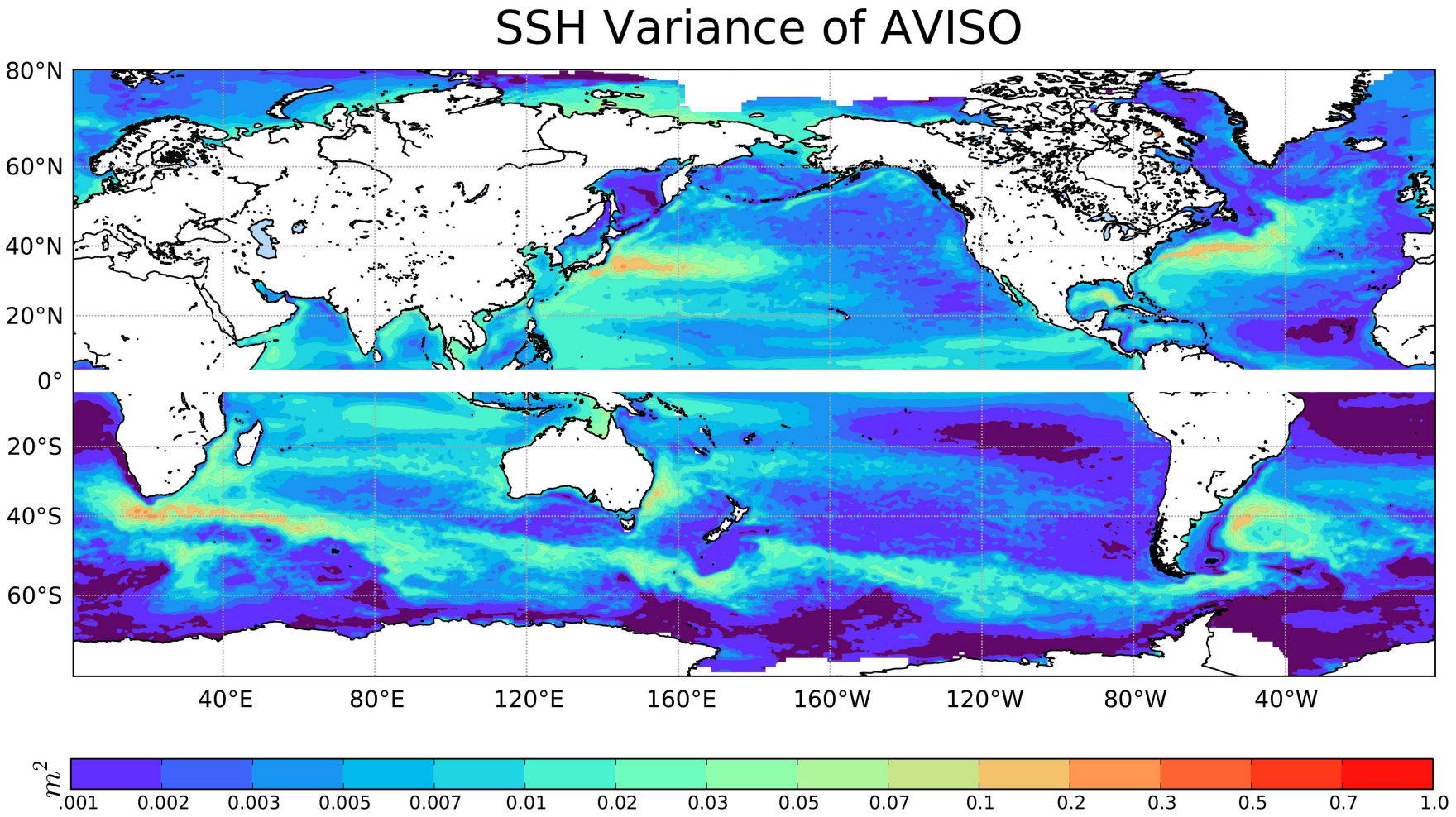

Figure 5: Sea Surface Height variance from AVISO altimetry, 1993-2007. Note the non-linear colour scale, dark violet shading indicates SSH variance $< 0.001 m^2$.

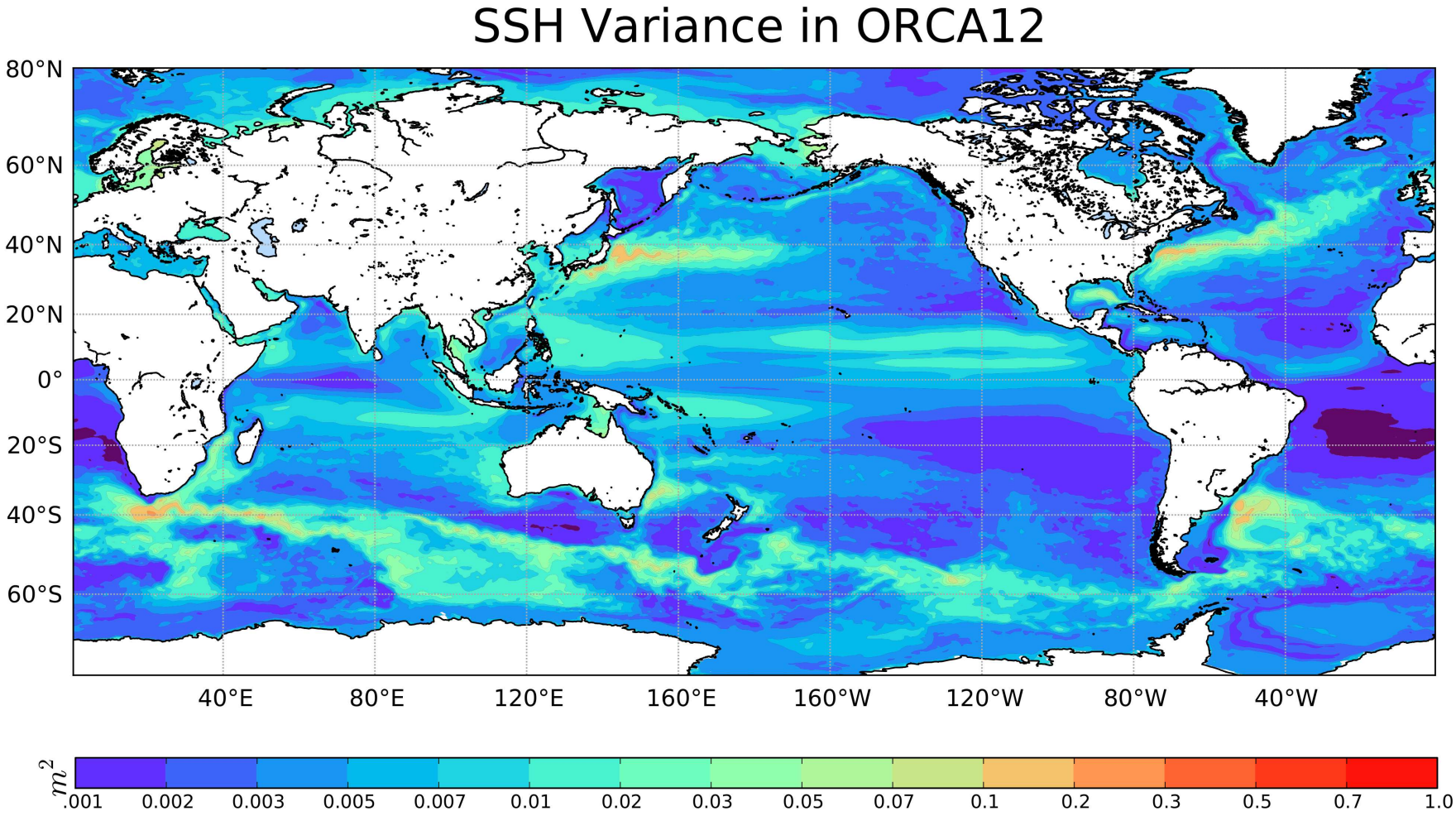

Figure 6: Sea Surface Height variance from ORCA12, 1981-2007. Note the non-linear colour scale, dark violet shading indicates SSH variance $< 0.001m^2$.

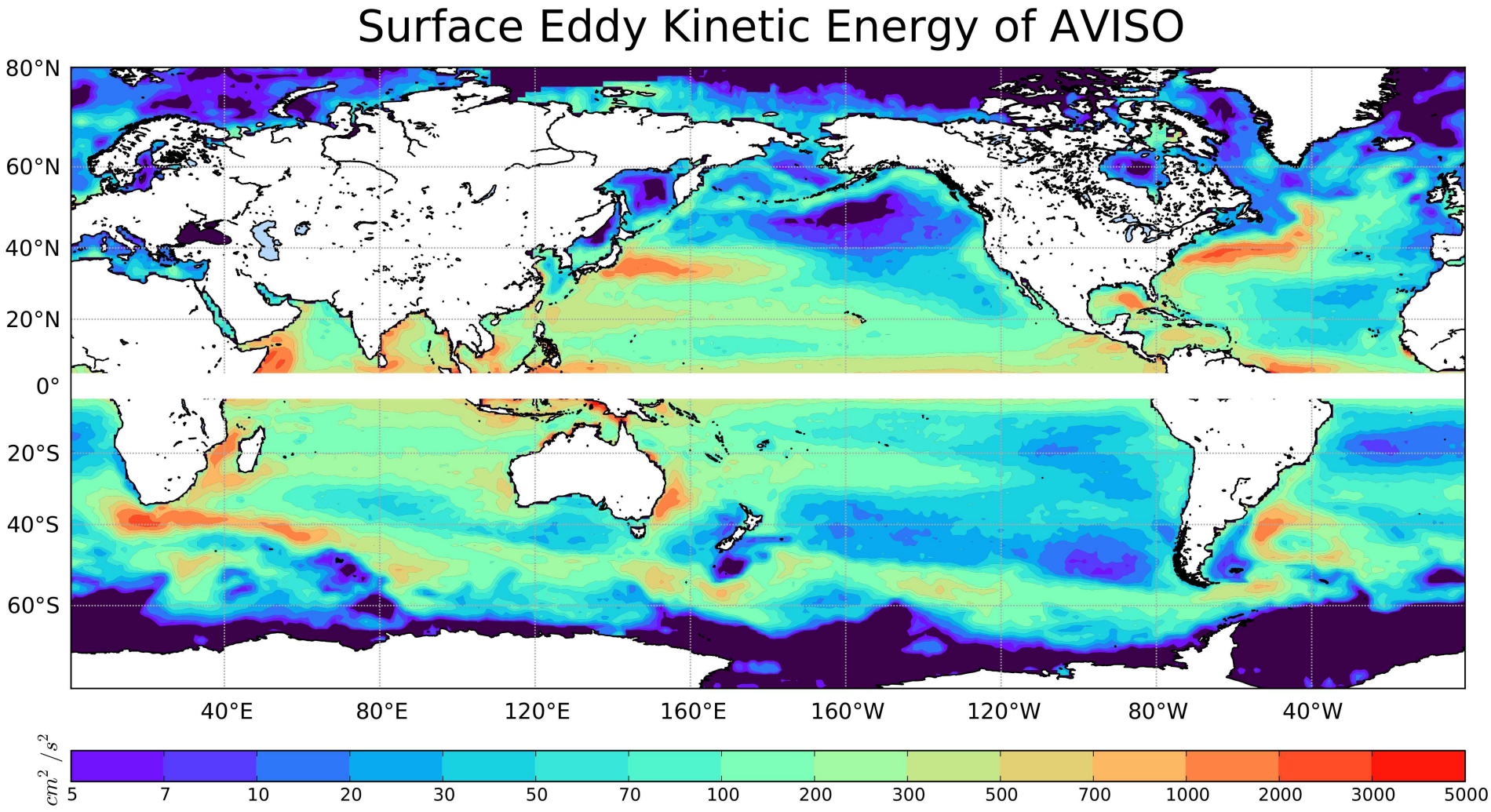

Figure 7: Mean geostrophic surface Eddy Kinetic Energy from AVISO SSH, 1993-2007. Note the non-linear colour scale, dark violet shading indicates EKE $< 5cm^2s^{-2}$.

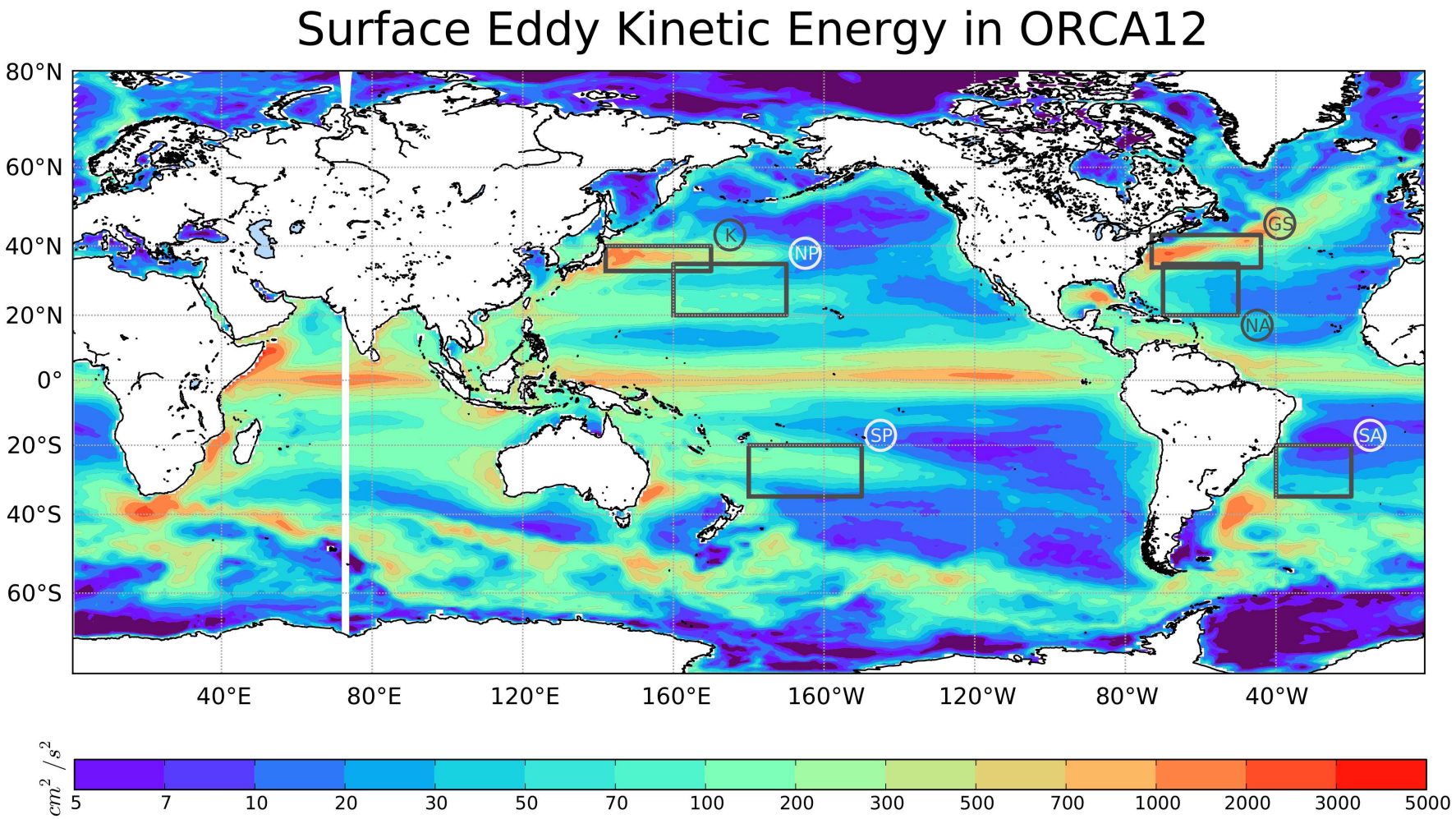

Figure 8: Mean surface Eddy Kinetic Energy from ORCA12, 1981-2007. Note the non-linear colour scale, dark violet shading indicates EKE $< 5cm^2s^{-2}$. Regions for further investigations are indicated by the boxes: (K): Kuroshio; (GS): Gulf Stream; (NP): North Pacific; (NA): North Atlantic; (SP): South Pacific; (SA): South Atlantic.

of equations (2) and (3) to calculate geostrophic velocities has to be taken into account, as the Coriolis parameter converges towards zero.

Over most of the interior of the subtropical oceans, values below $100 cm^2 s^{-2}$ are common, with local minima $< 50 cm^2 s^{-2}$ in the eastern parts of the subtropical gyres of the NA and North Pacific (NP) and $< 10 cm^2 s^{-2}$ in their southern counterparts. In the vicinity of current bands such as the Azores Current in the Atlantic and the North and South Equatorial Currents of the Pacific, elevated EKE levels of up to $500 cm^2 s^{-2}$ can be observed. EKE in all subpolar and polar oceans is generally low with minima $< 5 cm^2 s^{-2}$. The mean geostrophic EKE from 15 years of satellite altimetry is in good agreement with previous studies. Scharffenberg and Stammer (2010) used 4 years of altimetry data (2002-2005) and (Xu et al., 2011) used the same 15 years period (1993-2007) as this study, both showing no major differences to the AVISO-based EKE calculated here.

Figure 8 shows the mean EKE from the ORCA12 model output. The model reproduces the spatial distribution realistically. Highest EKE, $1000 cm^2 s^{-2}$ to over $3000 cm^2 s^{-2}$, is found in the GS, Kuroshio and Agulhas Retroflection. Larger differences can be found in the Indian Ocean, where ORCA12 EKE is generally higher than the geostrophic AVISO EKE. Additionally, values of $500 cm^2 s^{-2} - 1000 cm^2 s^{-2}$ can be found along the path of the ACC, which is also higher than in the AVISO data. The local minima of AVISO EKE are not as pronounced in the ORCA12 EKE, especially in the subpolar and polar regions. The EKE in the eastern South Pacific (SP) however is lower than in the satellite data with EKE $< 10 cm^2 s^{-2}$ being widespread.

Furthermore, the regions to be analysed in detail later are introduced in figure 8. Two regions including the Gulf Stream system (GS; $34°N - 43°N$, $44°W - 73°W$) and the Kuroshio/Kuroshio Extension system (K; $33°N - 40°N$, $142°E - 170°E$) have been chosen due to the high EKE levels there and to be compared to previous studies. The regions in the subtropical gyres (North Pacific (NP; $20°N - 35°N$, $160°E - 190°E$), North Atlantic (NA; $20°N - 35°N$, $50°W - 70°W$), South Pacific (SP; $20°S - 35°S$, $150°W - 180°W$), South Atlantic (SA; $20°S - 35°S$, $20°W - 40°W$)) were chosen due to the significance of the seasonal cycle (Fig. 10), described further in sections 4.1.3 and 4.1.4.

4.1.3 Amplitude of the Seasonal Cycle of Eddy Kinetic Energy

The distribution of the amplitude of the EKE's seasonal cycle in AVISO (Fig. 9) resembles that of the mean EKE (Fig. 7). Areas with a high mean EKE also show the largest amplitudes in the seasonal cycle. Consequently, amplitudes of $\sim 1000 cm^2 s^{-2}$ are found in the GS and Kuroshio regions as well as in seasonally varying currents like the NECC in the Atlantic and the Somali Current of East Africa. In these regions, it is most likely the seasonal cycle of $\overline{u}$ and $\overline{v}$ that leads to erroneous implications about the EKE. Though it cannot be ruled out, that also the EKE varies with the seasons. In the ACC, amplitudes of up to $500 cm^2 s^{-2}$ can be observed while again, lowest values are found in the subpolar and polar regions ($< 10 cm^2 s^{-2}$). The subtropical gyres have amplitudes between $< 5 cm^2 s^{-2}$ and $\sim 100 cm^2 s^{-2}$ with minima in the eastern parts. These findings are in agreement with previous studies, e.g. Scharffenberg and Stammer (2010) and Zhai et al. (2008). Note that the EKE in Zhai et al. (2008) is too high by a factor of two and has to be divided by this factor, to be comparable to this study (R. Greatbatch, pers. comm.).

The amplitude of the seasonal cycle of EKE in ORCA12 shows high similarity to the AVISO EKE. In figure 10, only regions with an amplitude of $\geq 150 cm^2 s^{-2}$ or, for values lower than $150 cm^2 s^{-2}$, an amplitude at least 30% of the mean are shown. Choosing only the '30% of the mean'-criterion rules out various regions with large mean EKE levels, although there are amplitudes well above $200 cm^2 s^{-2}$. Only inspecting regions showing a large amplitude in the absolute sense, on the other hand, rules out a lot of areas with low EKE levels, with amplitudes in the same order of magnitude as the mean. Therefore, a combination of both criteria is used.

The amplitude in the GS and Kuroshio regions is slightly lower in ORCA12 than in AVISO with values not exceeding $1000 cm^2 s^{-2}$. Most of the rest of the ocean basins show large agreement between AVISO and ORCA12. The subpolar and polar regions and the eastern subtropical gyres have very low amplitudes $< 10 cm^2 s^{-2}$. Interestingly, these fulfil the above mentioned criteria in vast areas around Antarctica, the SP and SA,

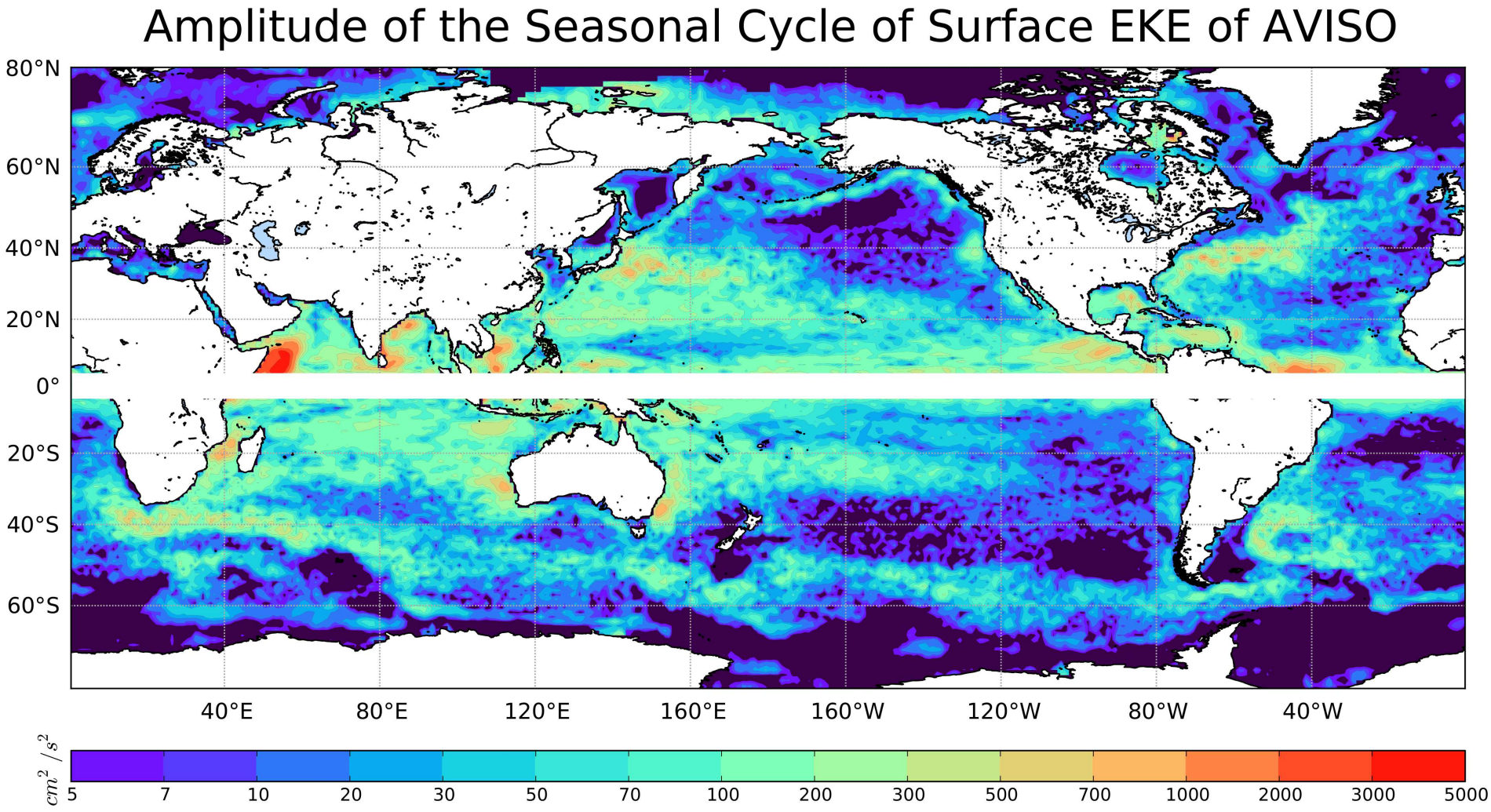

Figure 9: Amplitude of the mean seasonal cycle of geostrophic surface Eddy Kinetic Energy from AVISO SSH, 1993-2007. Note the non-linear colour scale, dark violet shading indicates EKE $< 5cm^2s^{-2}$.

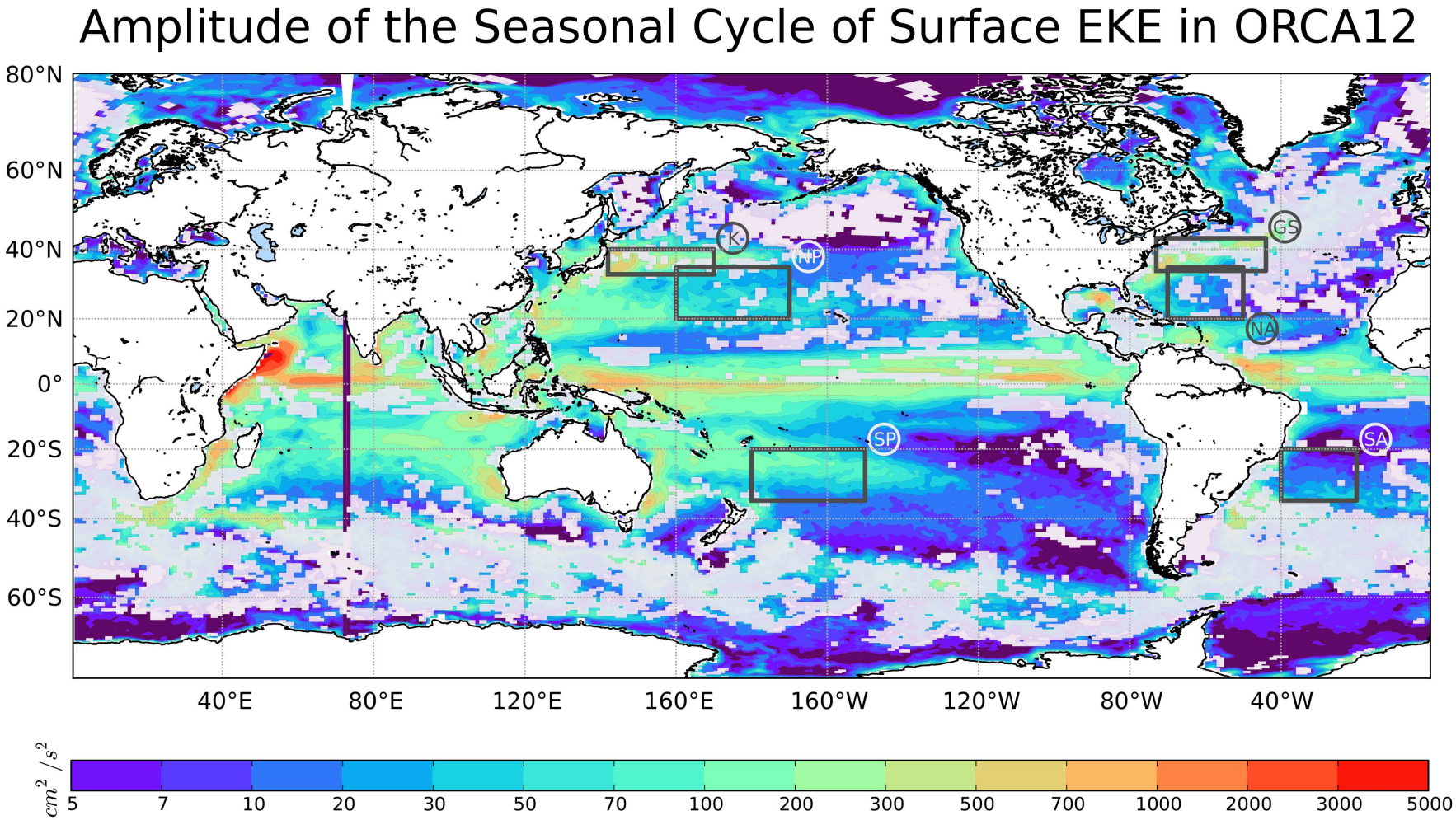

Figure 10: Amplitude of the mean seasonal cycle of surface Eddy Kinetic Energy from ORCA12, 1981-2007. Note the non-linear colour scale, dark violet shading indicates EKE $< 5cm^2s^{-2}$*. Regions for further investigations are indicated by the boxes: (K): Kuroshio; (GS): Gulf Stream; (NP): North Pacific; (NA): North Atlantic; (SP): South Pacific; (SA): South Atlantic. Regions with faded colors indicate an amplitude of the seasonal cycle of less than* $150cm^2s^{-2}$ *and smaller than 30% of the mean EKE.*

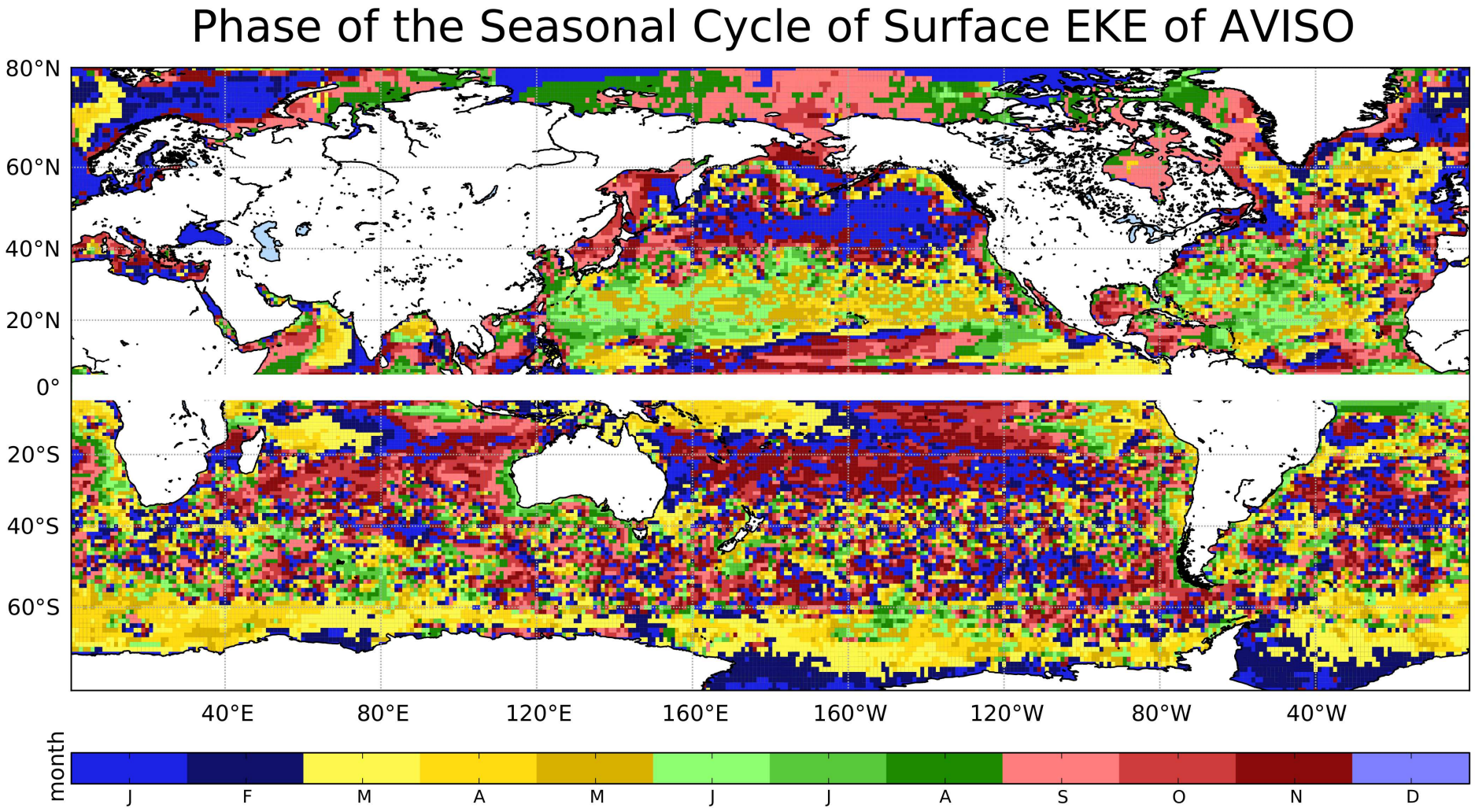

Figure 11: Phase of the mean seasonal cycle of geostrophic surface Eddy Kinetic Energy from AVISO SSH, 1993-2007.

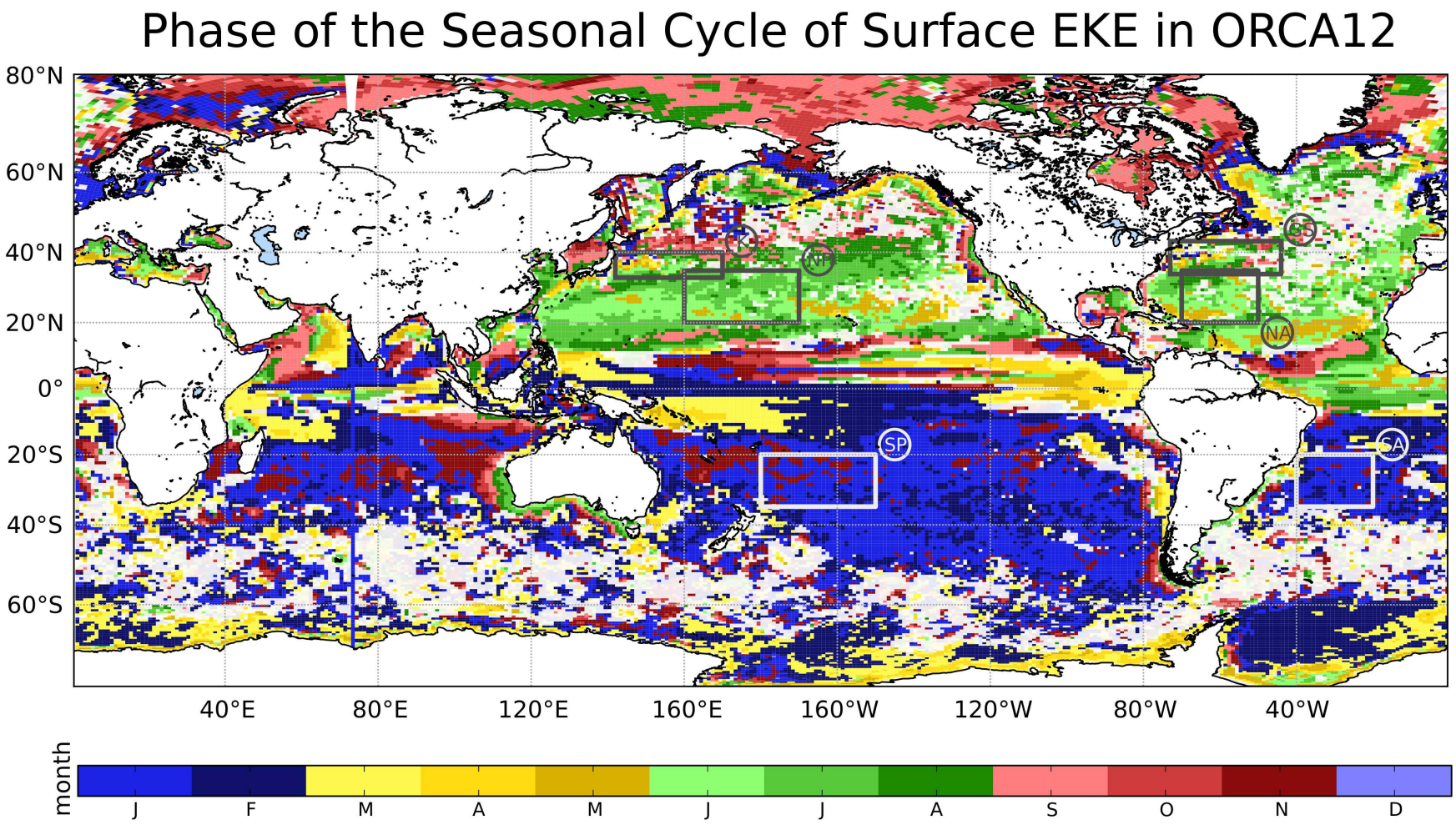

Figure 12: Phase of the mean seasonal cycle of surface Eddy Kinetic Energy from ORCA12, 1981-2007. Regions for further investigations are indicated by the boxes: (K): Kuroshio; (GS): Gulf Stream; (NP): North Pacific; (NA): North Atlantic; (SP): South Pacific; (SA): South Atlantic. Regions with faded colors indicate an amplitude of the seasonal cycle of less than $150cm^2s^{-2}$ *and smaller than* 30% *of the mean EKE.*

while in the NP and NA, regions with small amplitudes generally do not show a significant seasonal cycle. Some regions do not fulfil the significance criterion, despite they have a relatively high amplitude of the seasonal cycle. These regions include the whole Northeastern Altantic (NEA) and the ACC. The spatial distribution of regions showing a significant seasonal cycle in ORCA12 shows good agreement with figure 4(b) in Zhai et al. (2008). They show the seasonal cycle of EKE to be only a small portion of the total variability in most of the Southern Ocean and the NEA, while it has a large contribution in the subtropical regions.

4.1.4 Phase of the Seasonal Cycle of Eddy Kinetic Energy

The phase of the seasonal cycle of EKE, the month with the highest EKE, shows a symmetry about the equator in AVISO. While the midlatitude NH shows maximum EKE during May to August, the southern midlatitudes reach a maximum in November to February. Globally, south of $30°S$, no clear signal can be seen, except for a maximum in southern fall along the Antarctic continent. The NP subpolar gyre has a clear northern winter maximum in EKE, while in the subpolar NA the maximum of the seasonal cycle is located in spring. These results are similar to the ones by Zhai et al. (2008), who also had a long period of satellite data avialable (12 years). In other studies with shorter temporal data coverage, the results are contrasting. Scharffenberg and Stammer (2010) used 4 years of satellite data and found the phase of the seasonal cycle to be very heterogeneously distributed, although some similarities to this study can be seen. Additionally, Stammer and Wunsch (1999) found opposing seasonal cycles with winter/spring maxima in the NH subtropical regions.

The model reproduces the phase of the seasonal cycle remarkably well on a global scale. The symmetry about the equator is even more evident than in AVISO. The subpolar gyres have a spatially more homogeneous distribution of the phase of the EKE's seasonal cycle. This might be due to the longer time period of the model output which reduces noise levels. Highly spatially variable regions in the AVISO dataset are observed to show no significant seasonal cycle in ORCA12, e.g. the ACC and the NEA. Even small local features are represented in ORCA12. At the western and southern coast of Aus-

tralia the Leeuwin Current can be identified as a source for EKE for the Southern Indian Ocean (Scharffenberg and Stammer, 2010) with a southern winter maximum. A winter maximum is also observed along the Brazil Current. The only region with large discrepancies between AVISO and ORCA12 is the subpolar NA, where AVISO EKE shows a winter/spring maximum and ORCA12 has a maximum in summer.

Summarizing the findings of the global comparison, it becomes clear that ORCA12 does reproduce the observed EKE levels and its seasonal cycle remarkably well, especially in the regions of interest here, the midlatitudes. Because there are some minor differences concerning the exact locations of currents, especially the WBCs and its extensions, a direct, quantitative comparison in the form of correlations etc. on a global scale is not prone to deliver satisfying results. Therefore, this direct comparison is performed on a regional scale in section 4.2 for the WBCs and section 4.3 for the subtropical gyres' interior.

4.2 Western Boundary Currents

After evaluating the model's performance on a global scale, the WBCs in the NH will now be examined in detail. The GS, as well as the Kuroshio and its extension show similar behavior of the mean EKE. Maximum levels are found in the western parts, near the separation points, with more than $2000 cm^2 s^{-2}$ (Fig. 13 (a) and (b)). EKE levels between $500 cm^2 s^{-2}$ and $1000 cm^2 s^{-2}$ are extending as far east as $40°W$ in the GS and $165°E$ in the Kuroshio. Compared to observations, both currents are too far north at their separation points by roughly 2° (Brachet et al., 2004; Ducet and Le Traon, 2001; Zhai et al., 2008). The GS shows a second maximum in mean EKE located around $43°N$, $45°W$ with values $> 1000 cm^2 s^{-2}$, which is also observed in the satellite data, but the area between $50°W$ and $60°W$ has too low EKE in ORCA12 (maximal differences to observed EKE $\sim 2000 cm^2 s^{-2}$, compare Brachet et al. (2004)). The Kuroshio, in comparison to the GS, shows a strictly zonal extension and a quasi-stationary meander between $142°E$ and $153°E$. This has also been observed by satellite altimetry (Qiu, 2002).

The amplitudes of the EKE's seasonal cycles (Fig. 13 (c) and (d)) are largest in the

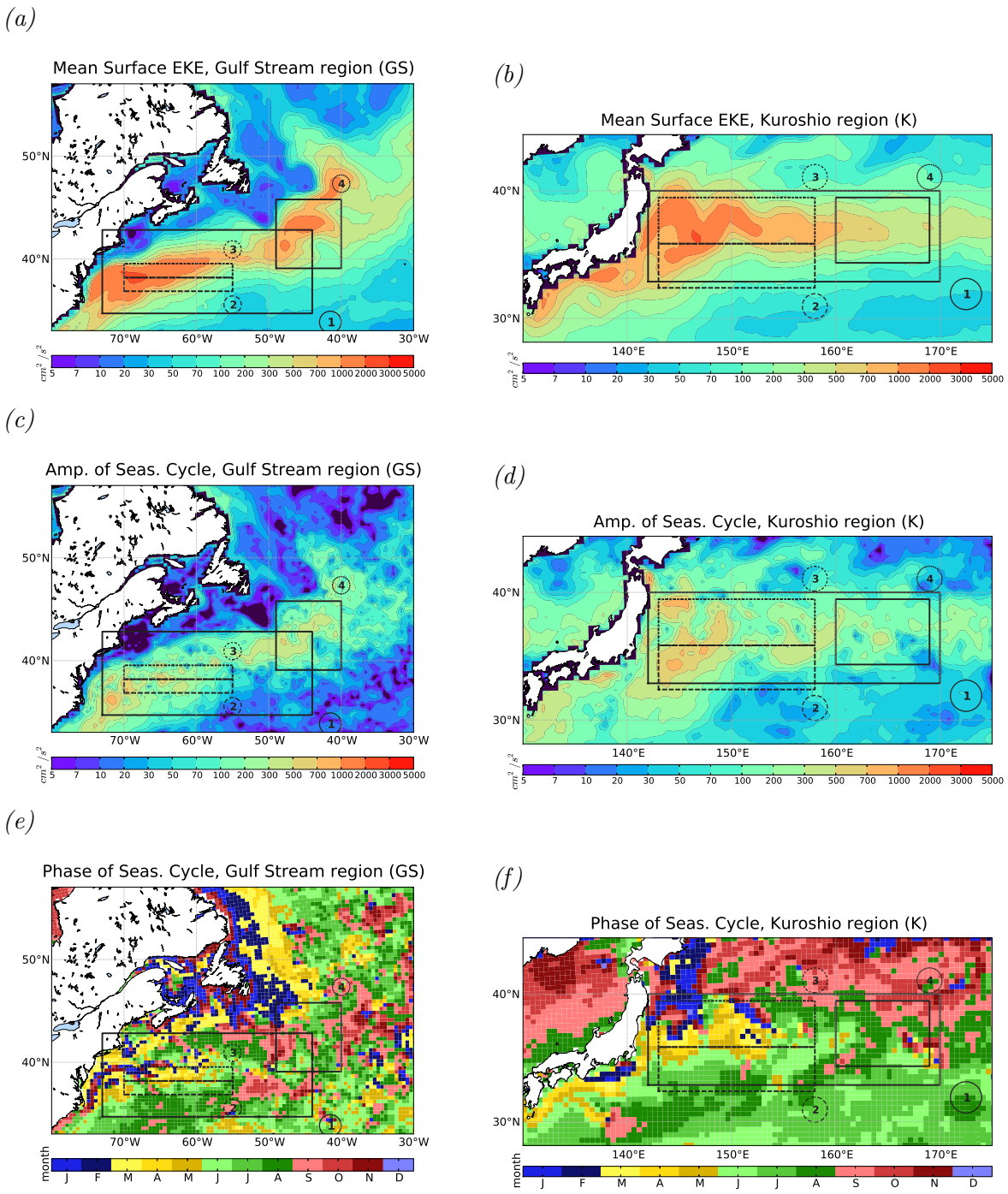

Figure 13: Mean surface EKE from ORCA12 (top) for the Gulf Stream region (a) and the Kuroshio region (b), amplitude of the seasonal cycle of surface EKE (middle) for GS (c) and Kuroshio (d) and phase of the seasonal cycle of surface EKE (bottom) for GS (e) and Kuroshio (f). Lines in (a)-(f) show the boxes used for later investigations. Box (1): solid; box (2): dashed; box (3): dash-dotted; box (4): dotted. The color scale in (e) and (f) indicates the month with maximum EKE from January through to December.

eastern parts of both WBCs, near the separation point. Amplitudes of $500cm^2s^{-2}$ and more are found between $64°W$ and $72°W$ in the GS and between $142°E$ and $149°E$ in the Kuroshio, where the amplitude is slightly higher than in the GS. Amplitudes of more than $100cm^2s^{-2}$ are found as far east as $40°W$ in the GS and $175°E$ in the Kuroshio.

Regarding the phase of the EKE's seasonal cycle, it has already been shown (Fig. 12) to be in general agreement with previous studies, showing a summer maximum in the subtropical oceans. Various studies also found this to apply for the GS (Brachet et al., 2004; Ducet and Le Traon, 2001; Stammer and Wunsch, 1999; Zhai et al., 2008) and Kuroshio (Adamec, 1998; Ducet and Le Traon, 2001) regions. The ORCA12 model with its high resolution of 1/12° and relatively long time period of 26 years allows a more detailed investigation, as less spatial smoothing is required. This reveals some intriguing local features shared by both, the GS and the Kuroshio. Embedded in a background of summer maxima in the subtropical gyres, the cores of the WBCs, after their separation from the coast, show a winter maximum in EKE at their northern margins and a spring maximum at their southern margins (Fig. 13). This feature extends to the east to $58°W$ in the GS and $153°E$ in the Kuroshio. The eastward extend approximately correlates with the eastward extend of mean EKE levels $> 1000cm^2s^{-2}$ in both WBCs.

(a) *(b)*

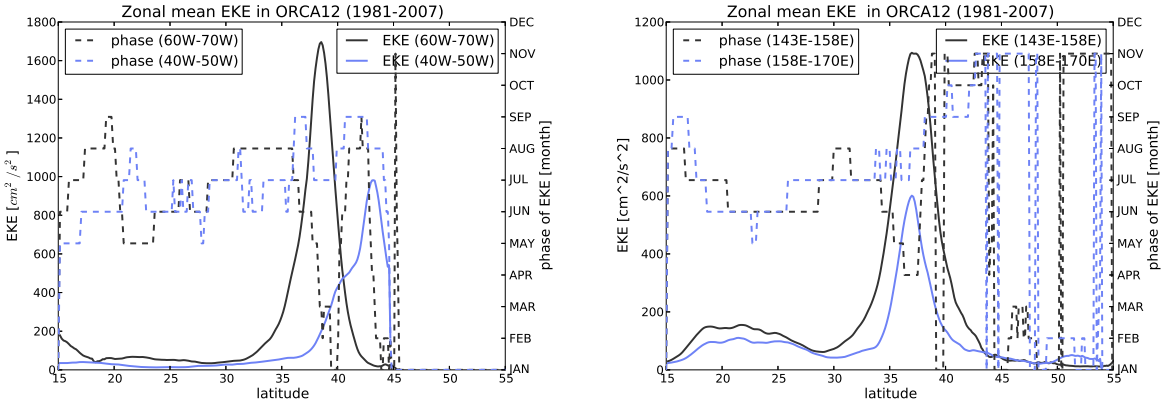

Figure 14: Sections of zonal mean EKE against latitude in the North Atlantic (a) and North Pacific (b). Solid lines indicate zonal mean EKE averaged over the western parts of the WBCs (black), $60°W-70°W$ in the NA (a) and $143°E-158°E$ in the NP (b), and the eastern parts of the WBCs (blue), $40°W$ to $50°W$ in the NA (a) and $158°E-170°E$ in the NP (b). Dashed lines show the zonal mean phase for the western (black) and eastern (blue) parts. Months of the phase are indicated at the right.

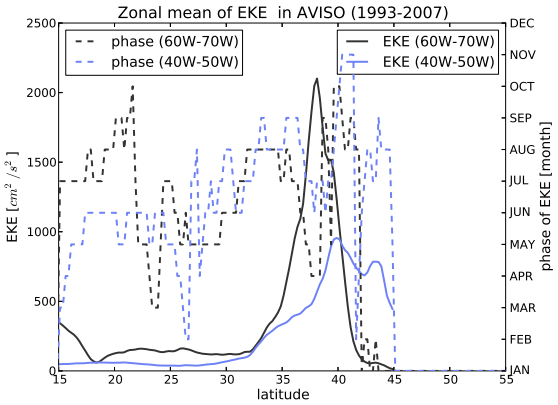

Figure 15: as figure 14 (a) but for AVISO data

Further downstream of both currents, the phase shifts towards later months in the year with longitude. Latest maximum EKE is found in September/October east of $50°W$ in the GS and $163°E$ in the Kuroshio.

To further illustrate this, figure 14 shows sections of zonal mean EKE for the western and eastern parts of the GS and the Kuroshio. In the western NA subtropical gyre EKE is below $100cm^2s^{-2}$ south of $33°N$, accompanied by a maximum of the seasonal cycle ranging from May to August. North of $33°N$ EKE rises to over $1500cm^2s^{-2}$ with a maximum at $38°N$, which can be seen as the core of the GS. This EKE maximum is accompanied by a phase shift towards spring and winter further north up to $40°N$. North of this minimum, the phase shifts back to August with EKE dropping to $< 100cm^2s^{-2}$ again at $42°N$. A similar behaviour, though not as pronounced, is seen by Scharffenberg and Stammer (2010) in their figure 21, although they do not comment on this.

The situation in the NP is almost identical. Low EKE with a maximum in the summer months (May to August) south of $33°N$ is followed further north by a steep incline in EKE from $32°N$ to $37°N$ which also coincides with a phase shift towards spring. Declining zonal mean EKE between $37°N$ and $43°N$ is then accompanied by an EKE maximum in winter (November to February). North of the Kuroshio however, the phase remains in winter months in contrast to the GS region. This difference though is not too surprising, as the GS is bounded by the North American continent/shelf towards the North, while the open North Pacific Ocean is located north of the Kuroshio.

In both WBCs, this phase shift towards winter in the core is only observed in the western parts with high EKE. Further to the east, where EKE levels are below $1000cm^2s^{-2}$ in the zonal mean, the maximum of the seasonal cycle of surface EKE lies between July and September across the core of the current.

The zonal mean EKE in the North Atlantic derived from AVISO data is depicted in

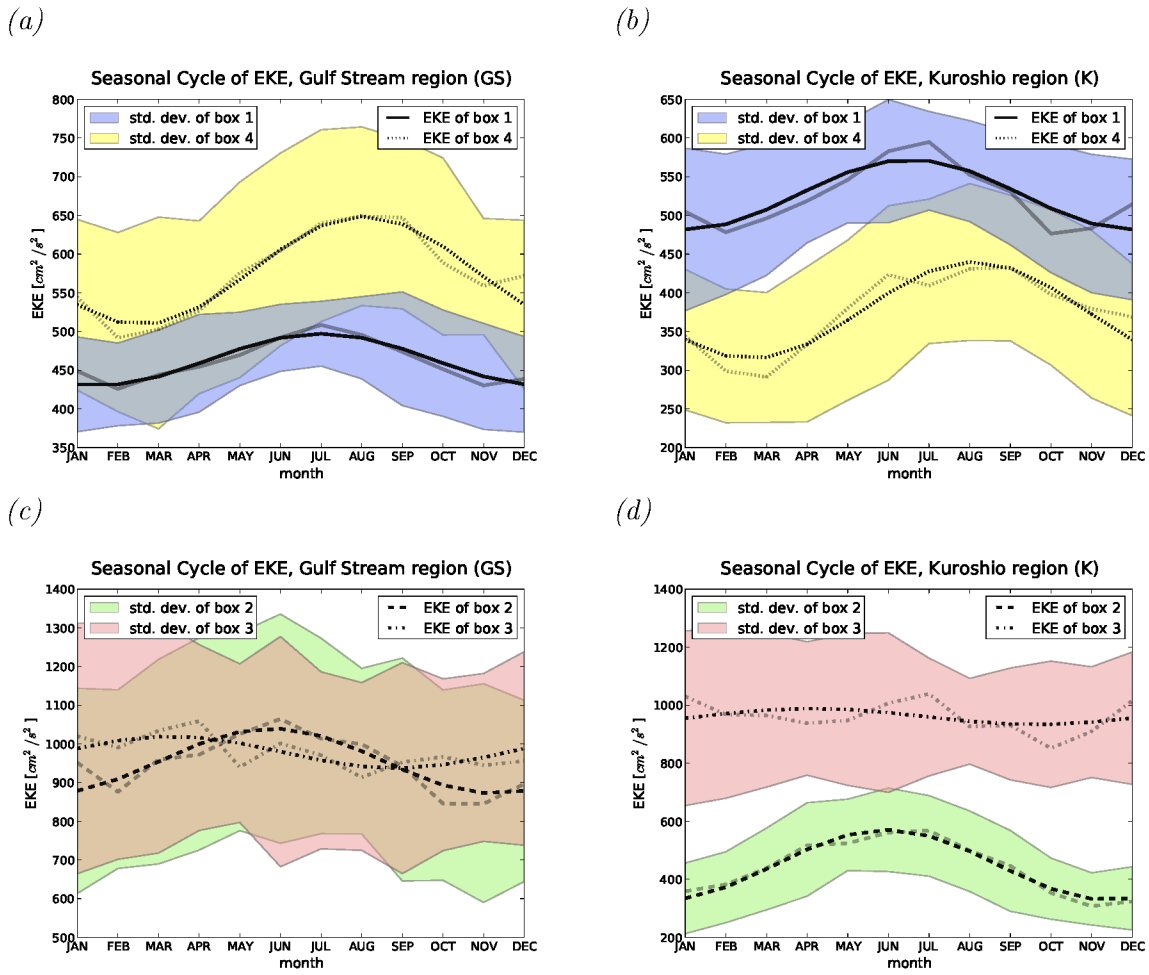

Figure 16: The seasonal cycles for the different boxes defined in figure 13. Solid lines are for box (1), the whole region; dashed lines for box (2), just south of the core of the WBCs; dash-dotted lines for box (3), containing the area with highest mean EKE and dotted lines for box (4), regions further downstream. The lighter curves represent the climatological monthly mean EKE and the bold curves the fitted seasonal cycle. The standard deviations are calculated in the time dimension to represent the interannual variability of the mean seasonal cycle and are illustrated as coloured shading (blue for box (1), green for box (2), red for box (3) and yellow for box (4)).

figure 15. In the subtropical gyre between $20°N$ and $33°N$, a low EKE with a maximum in summer is observed as well. In the vicinity of the GS however, the EKE is larger than in ORCA12, with a maximum of $> 2000 cm^2 s^{-2}$ at the core of the GS and the phase shift is not as pronounced. EKE has its maximum in spring in the GS but does not show a winter maximum at any latitude.

Looking more closely at the different boxes defined in figure 13 reveals that, when averaging over the whole region (box GS(1),K(1)), the widespread areas with a summer

maximum have the largest influence. In the GS, EKE peaks in July when averaged over box GS(1) (Fig. 16 (a)), the mean amplitude of the seasonal cycle however is rather small with $\sim 60 cm^2 s^{-2}$. In the Kuroshio the amplitude of the seasonal cycle in box K(1) is $\sim 110 cm^2 s^{-2}$. When averaging over box GS(4),K(4) further east, both, the GS and the Kuroshio, show a phase shift towards fall, as observed in previous figures. The mean EKE in box GS(4) of the GS area however is higher than that of box K(4) in the Kuroshio area. This is due to the maximum in EKE in the region where the GS turns towards the north, described in figure 13 (a).

The boxes GS(2),K(2) located just south of the WBCs cores are similar to the boxes GS(1),K(1) as they show a relatively robust summer (June) maximum (Fig. 16 (c) and (d)) with slightly higher amplitude of $\sim 150 cm^2 s^{-2}$. The interannual variability, illustrated by the standard deviation of the time mean seasonal cycle, is twice as large in the GS as in the Kuroshio region. Regarding the winter/spring maximum in the cores of both WBCs, figure 16 (c) and (d) shows that, when averaging over these regions (boxes (3)), this phase of the seasonal cycle is associated with a very small amplitude, especially considering the large interannual variability. In the Kuroshio, this box (3) shows almost no seasonal cycle at all.

Both NH WBCs show a large variability of the seasonal cycle of surface EKE. Distinct local features such as the winter/spring maximum in areas with highest mean EKE near their separation points clearly separate these regions from the surrounding summer maximum characteristic for the subtropical gyres.

4.3 Subtropical Gyres

In contrast to the highly variable GS and Kuroshio, the interior of the subtropical gyres shows a considerably lower EKE level and a spatially rather homogeneous distribution of the phase of the seasonal cycle. First, the regions adjacent to the NH WBCs will be investigated in section 4.3.1, later in section 4.3.2 their SH counterparts will be compared.

4.3.1 Northern Hemisphere

The surface EKE in the subtropical gyres' interior is generally low compared to regions with strong current bands. In the NA box NA(1) ($20°N - 35°N$, $50°W - 70°W$), the mean EKE is $\sim 30 cm^2 s^{-2}$ with lowest levels in the east and higher values of $70 cm^2 s^{-2} - 100 cm^2 s^{-2}$ in the western parts, close to the GS (Fig. 17 (a)). The mean EKE shows no significant meridional changes. In the NP box NP(1) ($20°N - 35°N$, $160°E - 190°E$), the northern part (box NP(3)) is similar to its Atlantic counterpart with EKE levels of $\sim 50 cm^2 s^{-2}$ and no major zonal differences (Fig. 18 (a)). In the southern part (box NP(2)) however, a zonal band of elevated EKE levels ($\sim 100 cm^2 s^{-2}$) is observed, that is probably associated with the Subtropical Counter Current.

The distribution of the amplitude of the seasonal cycle resembles that of the mean EKE. A small amplitude of $5 cm^2 s^{-2} - 30 cm^2 s^{-2}$ is found in the NA with higher values towards the eastern margins of the region (Fig. 17 (b)). The amplitude in the NP is generally higher than in the NA, ranging from $20 cm^2 s^{-2} - 50 cm^2 s^{-2}$ in the northern part (box NP(3)) and $30 cm^2 s^{-2} - 100 cm^2 s^{-2}$ in the southern part (box NP(2), Fig. 18 (b)).

Despite the different dynamical settings of the two regions (NA and NP) with the Subtropical Counter Current in the Pacific, the phase of the seasonal cycle of surface EKE is very similar. Maximum EKE is found in a range from May to August almost everywhere in the investigated regions (box NA(1),NP(1), Fig. 17 (c) and Fig. 18 (c)), as observed in geostrophic EKE from satellite altimetry (Scharffenberg and Stammer, 2010; Zhai et al., 2008). In the NA, the southern part (box NA(2)) shows more regions with maximum EKE in May and June, while in the northern part (box NA(3)) phases of July and August are common. This difference is also evident in the NP, although not as pronounced.

These qualitative inspections are supported by some more quantitative investigations of the mean seasonal cycles averaged over the different boxes (Fig. 17 (d) and Fig. 18 (d)). In the NA, when averaging over the whole region (box NA(1)), the seasonal cycle has an amplitude of little more than $20 cm^2 s^{-2}$ and a maximum in July. Boxes NA(2) and NA(3) both have a smaller amplitude of $15 cm^2 s^{-2}$ and a phase in May/June for the southern box and July/August for the northern box. The general impression in the NP

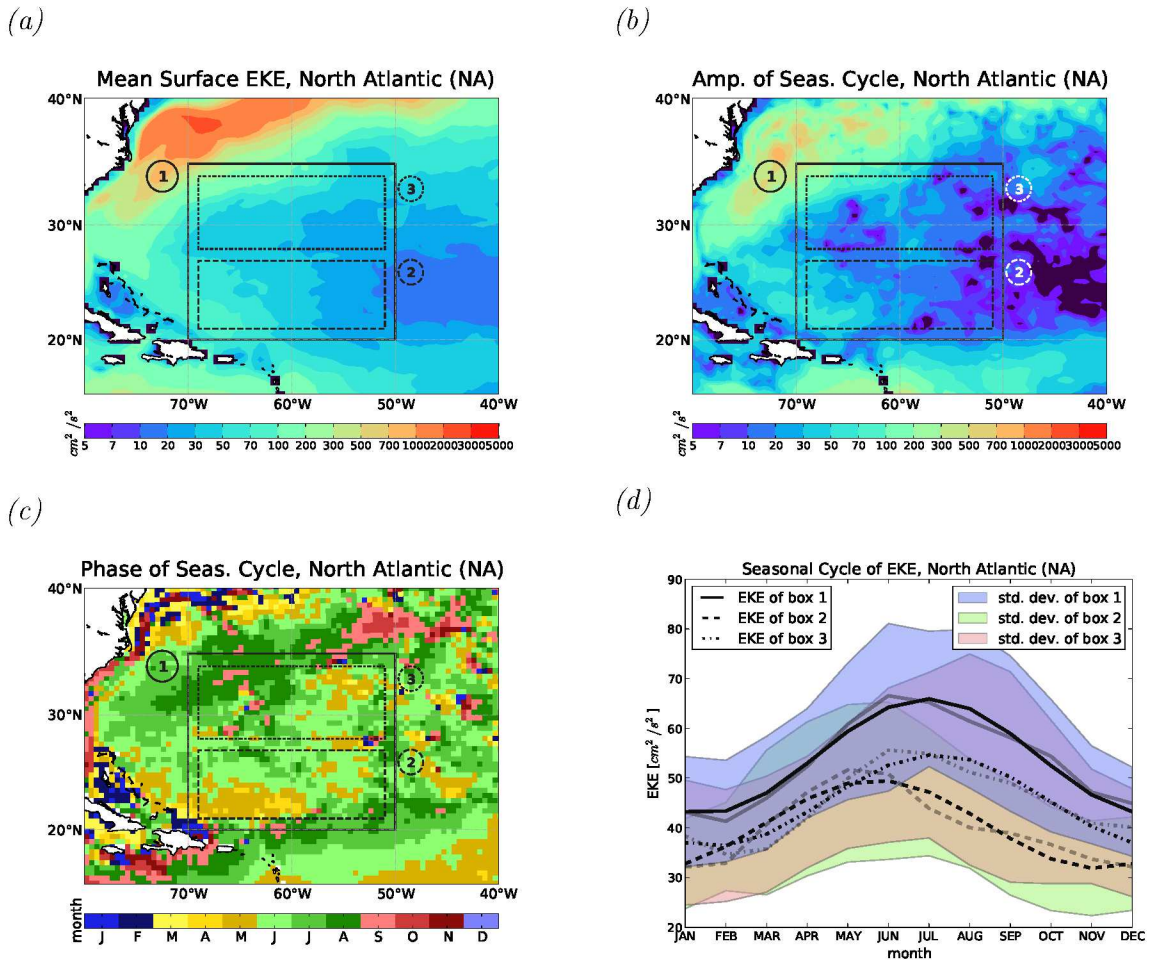

Figure 17: EKE and the seasonal cycle in the North Atlantic (NA), the phase in (c) has been binned into 0.5° bins. The seasonal cycles in (d) are for the different boxes in (a), (b) and (c). Solid lines are for box (1), dashed lines for box (2), dash-dotted lines for box (3). The lighter curves represent the climatological monthly mean EKE and the bold curves the fitted seasonal cycle. The standard deviations are calculated in the time dimension to represent the interannual variability of the mean seasonal cycle and are illustrated as coloured shading (blue for box (1), green for box (2), red for box (3) and yellow for box (4)).

is very similar, although the mean EKE levels and the amplitudes of the seasonal cycles are higher. Furthermore, the interannual variability is lower than in the NA. Averaging over the box NP(1), the resulting seasonal cycle has an amplitude of $35cm^2s^{-2}$ with a maximum in June/July. Box NP(2) in the south shows a larger amplitude of $40cm^2s^{-2}$ with a maximum in June and box NP(3) has a smaller amplitude of $25cm^2s^{-2}$ with a maximum in July.

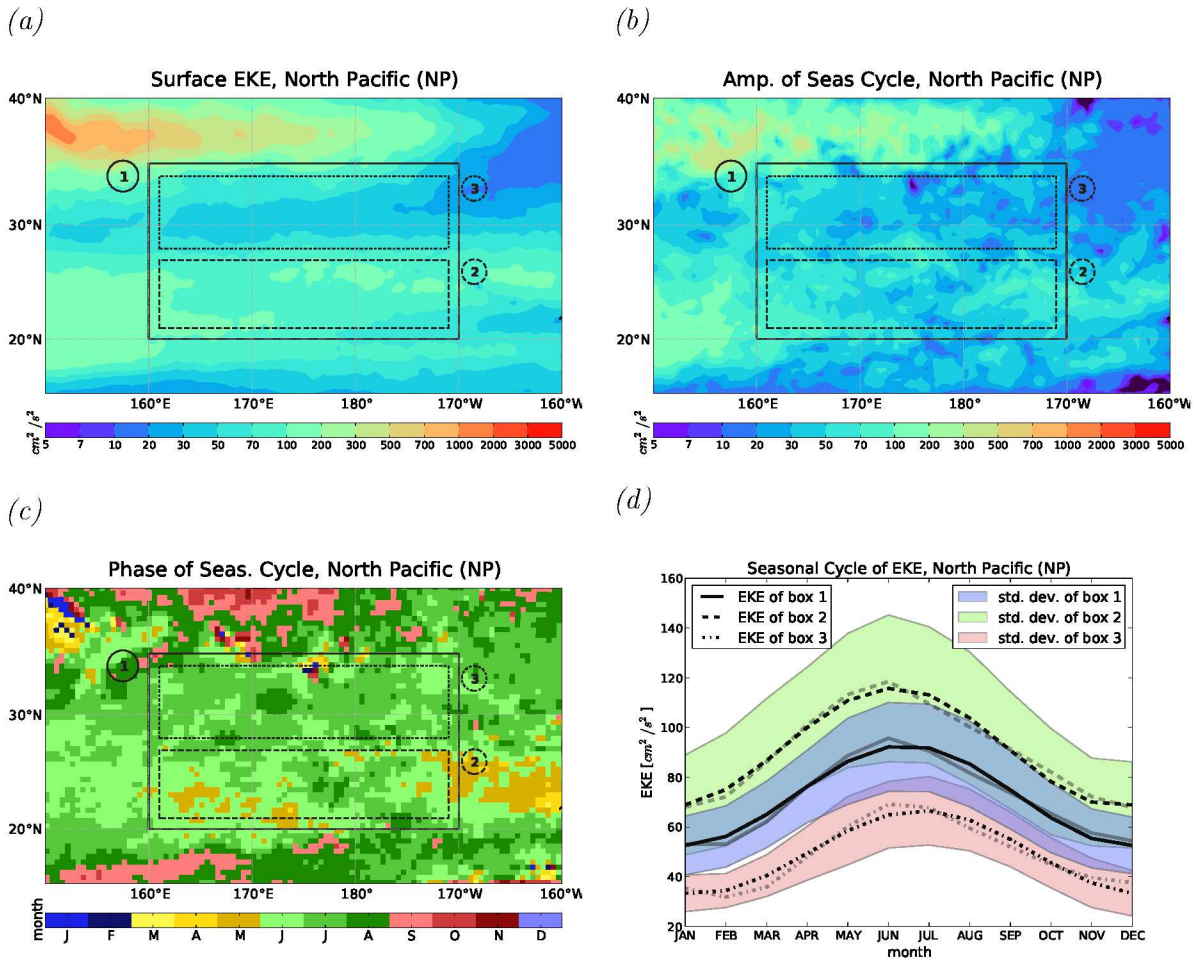

Figure 18: as figure 17, but for the North Pacific (NP).

4.3.3 Southern Hemisphere

In section 4.1, the symmetrical behaviour of the seasonal cycle of surface EKE about the equator was already shown. In this section it will be examined in more detail.

As in the NH, the SH subtropical gyres of the Atlantic and Pacific show generally low levels of mean EKE (Fig. 19 (a) and Fig. 20 (a)). The SA ($20°S-35°S$, $20°W-40°W$) exhibits mean EKE of $5cm^2s^{-2} - 30cm^2s^{-2}$ in the northern part (box SA(2)) and slightly higher levels in the southern part ($30cm^2s^{-2} - 50cm^2s^{-2}$). The detailed investigation in the SP ($20°S - 35°S$, $150°W - 180°W$) reveals an identical situation to the NP. A band of higher mean EKE ($50cm^2s^{-2} - 100cm^2s^{-2}$) is located in the equatorward area of box SP(1) and lower values of $10cm^2s^{-2} - 50cm^2s^{-2}$ further away from from the equator. As in the NH, mean EKE is higher in the Pacific, compared to the Atlantic.

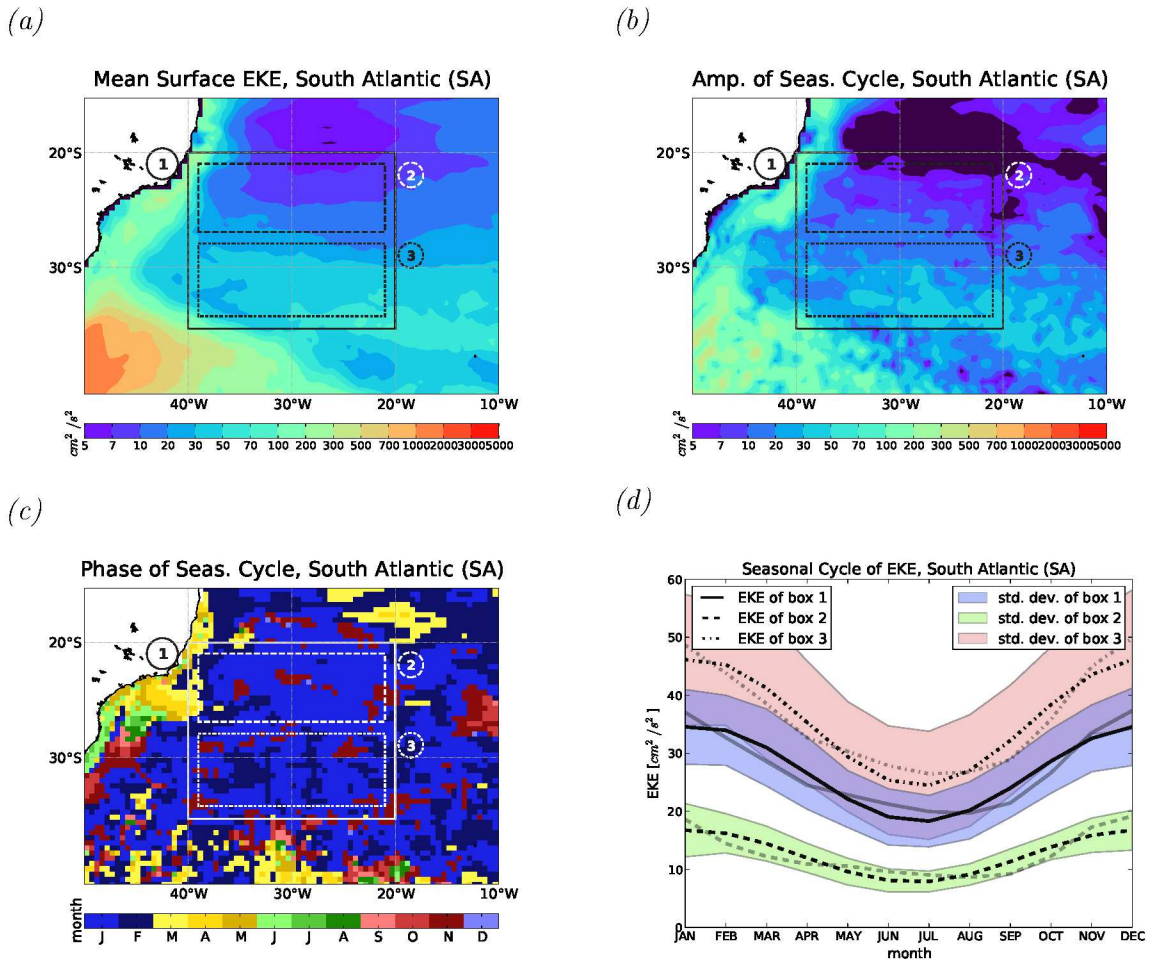

Figure 19: as figure 17, but for the South Atlantic (SA.)

The amplitude of the seasonal cycle of surface EKE in the SH subtropical gyre is closely connected to the mean EKE (Fig. 19 (b) and Fig. 20 (b)), as in the NH. In the SA the amplitude is lower than the mean with values reaching from $< 5cm^2s^{-2}$ in the northern part to $50cm^2s^{-2}$ at the southern margins of box SA(1). In contrast, the SP region shows an amplitude of the seasonal cycle that is as high as the mean in the whole region (box SP(1)).

The phase of the seasonal cycle, as in the NH, is astonishingly similar in the Atlantic and Pacific (Fig. 19 (c) and Fig. 20 (c)), although the distribution of mean EKE and amplitude of the seasonal cycle does show differences between northern (boxes SA(2),SP(2)) and southern (boxes SA(3),SP(3)) regions. Both, the SA and SP, have maximal EKE levels from November to February. In contrast to the NH subtropical gyres, there is no

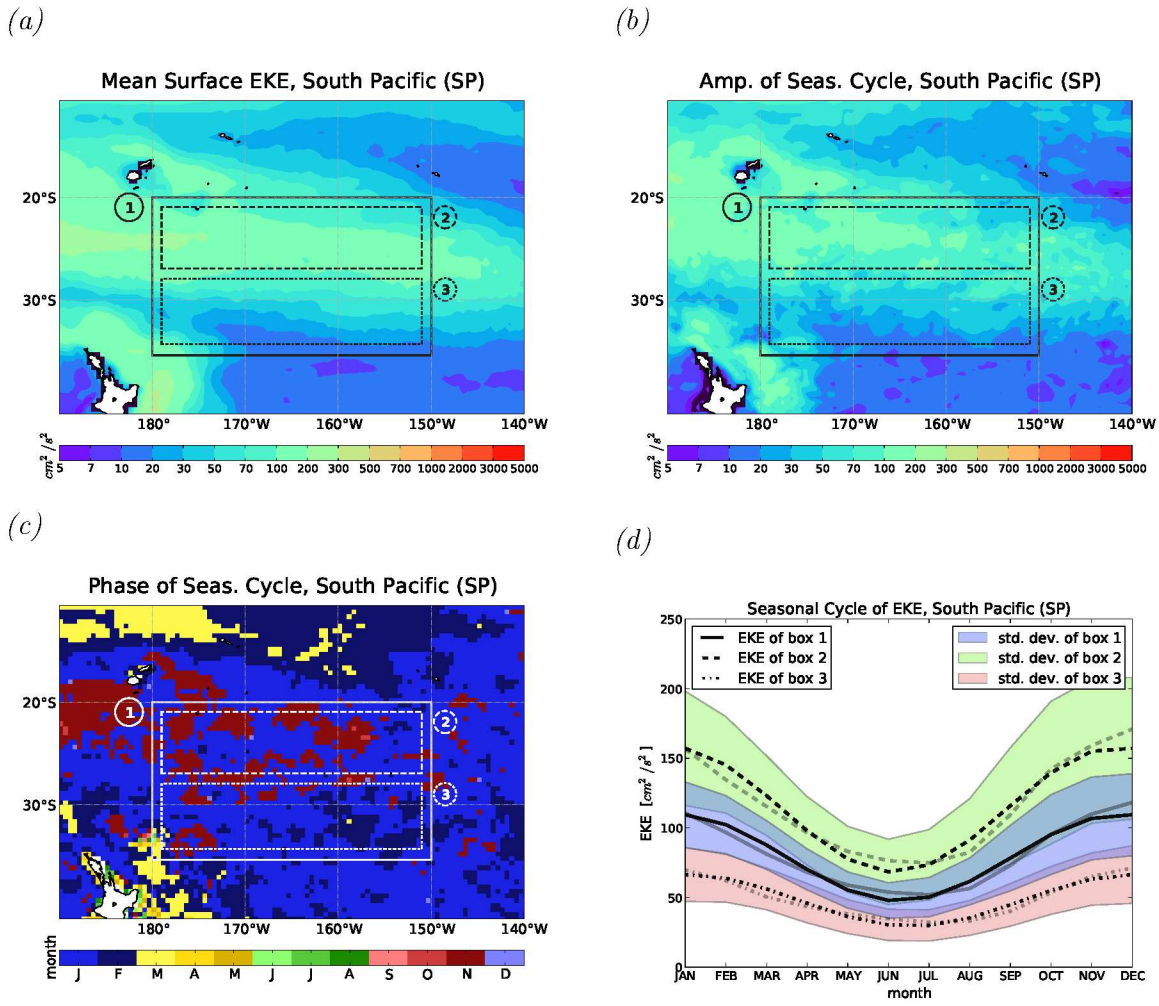

Figure 20: as Fig. 17, but for the South Pacific (SP).

obviously visible regional pattern of the phase (cf. the phase shift towards earlier months closer to the equator in figure 17 (c,d) and figure 18 (c,d)). Taking into account the global picture (Fig. 10), it can be argued that there is indeed such a shift in the SP with a phase of November around $20°S$ and February around $35°S$

Further, detailed inspection of the seasonal cycles averaged over the different boxes (Fig. 19 (d) and Fig. 20 (d)), reveals that all boxes in the SA and SP have their annual maximum EKE in December and January. Boxes SA(1),SA(2) and SA(3) show a very clean seasonal cycle in the SA. The fitted sine and the climatological mean values are almost identical. Averaging over the whole SA region (box SA(1)) gives a seasonal cycle with an amplitude of $15cm^2s^{-2}$, while box SA(3) has a slightly higher amplitude of $20cm^2s^{-2}$. The box SA(2), the one closer to the equator, has a very small amplitude

of only $8cm^2s^{-2}$ but also shows only marginal interannual variability. The SP boxes show a very similar behaviour with comparable or even lower interannual variability and amplitudes of roughly $60cm^2s^{-2}$, $90cm^2s^{-2}$ and $30cm^2s^{-2}$ for boxes SP(1),SP(2) and SP(3) respectively.

5 Discussion of Possible Mechanisms

To explain the observed seasonal cycles of surface EKE, different possible mechanisms are tested. The most important aspect of producing mesoscale eddy kinetic energy is the barotropic and baroclinic instability. Beckmann et al. (1994) see the velocity shear between the Mixed Layer and the interior oceans as crucial in generating eddy kinetic energy, especially in the interior of the subtropical gyres. This will be tested by investigating the mean seasonal cycle of vertical shear of velocity $\frac{\partial u}{\partial z}$, calculated from the mean seasonal cycle of velocities, averaged over the top $50m$ and from $50m - 500m$. If the seasonal cycle of EKE was in phase with the vertical shear, the seasonally varying generation of EKE could be responsible for this seasonal cycle.

Regarding the Gulf Stream System however, Zhai et al. (2008) found no correlation of the eddy production estimated by the eddy growth rate time scale with EKE levels observed. They suggest the dissipation of EKE being responsible for the expressed seasonal cycle, rather than the generation of EKE. Two possible mechanisms are discussed here, that could lead to a seasonal cycle in eddy dissipation rates and therefore the seasonal cycle of EKE itself.

First, the thermal capping of eddies due to a strong thermocline in summer is discussed. In summer, the thermocline decouples the eddies from the atmosphere, which strongly influences EKE through thermal interaction (Zhai and Greatbatch, 2006b) in winter, when high temperature differences between ocean and atmosphere lead to a strong damping. This mechanism is addressed by inspecting the mean seasonal cycle of the difference of potential density between $160m$ depth and the surface, derived from a monthly climatological density field. This indicates the strength of the decoupling of the surface mixed layer from the deeper ocean, which is assumed to have a constant density.

The second proposed mechanism to dissipate the EKE to a seasonally varying extend, is a direct mechanical damping exerted onto the eddies by wind stress. The wind stress is a function of the relative velocity between atmosphere and ocean. In regions where wind and ocean current point into the same direction, the wind stress is reduced compared to a case where the ocean is motionless. On the other hand, in regions where ocean currents and wind flow into opposite directions, the wind stress is enhanced. This reduction/enhancement by accounting for the relative motion between atmosphere and ocean however, has a non-linear effect. The magnitude of the reduction of wind stress is smaller, in an absolute sense, than the enhancement. Consequently, the wind stress dissipates EKE through its dependence on the relative motion. Furthermore, this damping itself is non-linearly connected to the wind speed, resulting in an exponential increase in wind stress with an increase in wind speed. As the wind stress is dependent on the wind speed directly, a larger damping of surface EKE is anticipated at times of higher wind speed (Zhai and Greatbatch, 2007). This will be tested by an investigation of the seasonal cycle of the monthly climatological magnitude of the wind stress $\tau = \sqrt{\tau_x^2 + \tau_y^2}$.

The focus will first be put on the subtropical gyre regions in section 5.1. The WBCs will be studied in detail in section 5.2.

5.1 Subtropical Gyres

5.1.1 Wind Stress Damping and Thermal Capping

The northern hemisphere subtropical gyres both show a clear seasonal cycle of surface EKE with a maximum in the summer months (Fig. 17 and 18). The seasonal cycle of the difference of potential density between $160m$ depth and the surface is similar in both ocean's subtropical gyres (Fig. 21 (a) and (b)), with a minimum in March and a maximum in August/September. In both, the NA and NP, the region closer to the equator (boxes NA(2),NP(2)) shows a less pronounced amplitude of the seasonal cycle. In spring, these annual cycles correspond to the theory of thermal capping being responsible for the elevated EKE levels in summer. The stratification starts to increase, decoupling the interior ocean from the atmosphere, in April. This roughly corresponds to the increase

in EKE in the NH subtropical gyres. However, the strong stratification does last until October and only then decreases, while EKE is already substantially lowered in October, compared to the summer. Furthermore, it is questionable whether the difference between air and sea temperatures is large enough, at least in the southern parts of the gyres, to significantly damp the EKE in winter.

The seasonal cycles of the difference between potential density at $160m$ depth and the surface in the SA and SP (Fig. 21 (c) and (d)) are comparable to the cycles in the NH. In SH late winter (August to October), the stratification shows a minimum. From October on, it exhibits a sharp increase with the development of the shallow summer Mixed Layer, before reaching its maximum in February/March. As for the NH this annual cycle cannot explain the full seasonal cycle of surface EKE through thermal capping in summer and thermal damping in winter. Stratification starts to increase substantially as late as October/November, while the surface EKE is already approaching its maximum in November.

The wind stress τ shows substantial differences between the various subtropical gyres. In the NA, τ has a semi-annual cycle which is less pronounced in the north (Fig. 21 (a)). Averaged over the whole region (box NA(1)), τ has its maximum in December/January with $0.07Nm^{-2}$, then decreases towards a local minimum in May/June ($< 0.04Nm^{-2}$). After this minimum, an increase is observed again until July ($> 0.05Nm^{-2}$). Later in the year a second local minimum is found in September/October (again $< 0.04Nm^{-2}$). This semi-annual cycle stands in clear contrast to the annual cycle of EKE. According to the the theory of wind work damping the EKE, a local minimum of EKE in July should be observed at least in the southern region of the NA (box NA(2)). However, it is possible that the higher stratification in summer leaves the wind work ineffective in damping the EKE. A combination of both, the damping through wind work in winter and the thermal capping in summer, could be responsible for the observed annual cycle of EKE. An inspection of the other subtropical gyres shows that such a connection cannot be established in general.

In the NP for example (Fig. 21 (b)), the seasonal cycle of τ has a strong maximum ($0.14Nm^{-2}$) in January in the northern region (box NP(3)), followed by values below

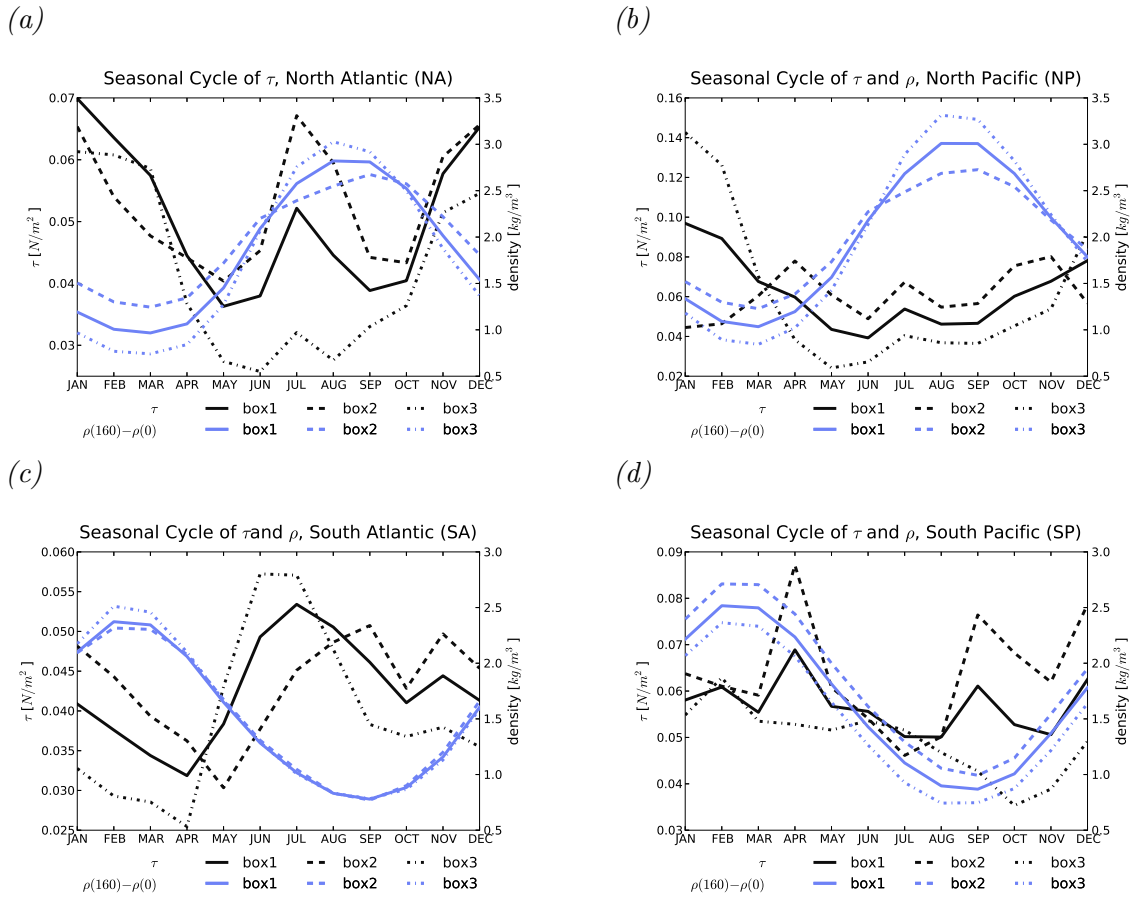

Figure 21: Mean seasonal cycles for the density difference between 160m depth and the surface (blue) as an indicator of the strength of the stratification and the wind stress (black). Averaged over different boxes shown in figures 17-20 for the North Atlantic (top left), North Pacifc (top right), South Atlantic (bottom left) and South Pacific (bottom right).

$0.05Nm^{-2}$ from April through to October. Thus it exhibits a large amplitude of the seasonal cycle with a phase that supports the wind work damping hypothesis. In contrast, the southern region (box NP(2)) has no seasonal cycle at all, with τ between $0.04Nm^{-2}$ and $0.08Nm^{-2}$ throughout the year, with maxima in April and October/November. Figure 18 shows both boxes, NP(2) and NP(3), have a very similar annual cycle of surface EKE, only differing in the mean. The wind work seems to have no clear influence on the EKE on a seasonal time scale in the NP, as two sub-regions with totally different temporal variability of τ show astonishingly similar annual cycles of EKE.

The wind stress in the SA is generally $< 0.06Nm^{-2}$ (Fig. 21 (c)), comparable to the NA. The wind stress τ in the northern part (box SA(2)) is $< 0.05Nm^{-2}$ throughout

the year with a minimum of $0.03 Nm^{-2}$ in May, while the southern part (box SA(3)) has a clear maximum of τ in June/July and $\tau < 0.04 Nm^{-2}$ for the rest of the year. In the SP τ is larger than in the SA on average (Fig. 21 (d)), comparable to the NH. Box SP(2) in the SP has maxima of $\tau \sim 0.08 Nm^{-2}$ in April, September and December with minima in between these months, the strongest being in July ($< 0.05 Nm^{-2}$). Box SP(3) in contrast, shows lower levels of $\tau < 0.06 Nm^{-2}$ with a minimum in October/November ($< 0.04 Nm^{-2}$) and a weak maximum in February. As for the NH, the annual cycles of wind stress show considerably differing behaviour for the different boxes, while the seasonal cycles of surface EKE are remarkably similar.

To summarize, the findings of this section suggest the seasonal cycle of surface EKE in the investigated subtropical gyre regions not to be influenced significantly by the annual cycles of stratification and wind stress. Possible explanations for the observed behaviour include the heat fluxes and wind work being too low in the subtropical gyres to substantially damp the surface EKE. Wind stress in the investigated regions is two to four times lower than in the WBC regions and the dissipation time scale for temperature anomalies in the NA is also estimated to be about five times as high as in the GS region (Zhai and Greatbatch, 2006a).

5.1.2 Vertical Shear and Velocity Profiles

The dissipation of EKE through atmospheric forces, the wind stress and heat flux, does not seem to be responsible for the observed annual cycle of EKE. Therefore, the hypothesis of local baroclinic instabilities being responsible for the EKE in general, and the seasonal cycle of EKE in particular, is tested in this section. The vertical shear of horizontal velocity is used as an indicator for these instabilities.

In the NA and NP, the vertical shear of horizontal velocity in the top $50m$ clearly peaks in the summer months (Fig. 22 (a) and (b)) with maxima in June/July between $0.3 \times 10^{-3} s^{-1}$ and $0.4 \times 10^{-3} s^{-1}$, which is followed by a rapid decrease until September. Throughout the winter months, the shear is close to zero in the top $50m$. In February/March a rather gradual increase towards the summer maximum is observed. The

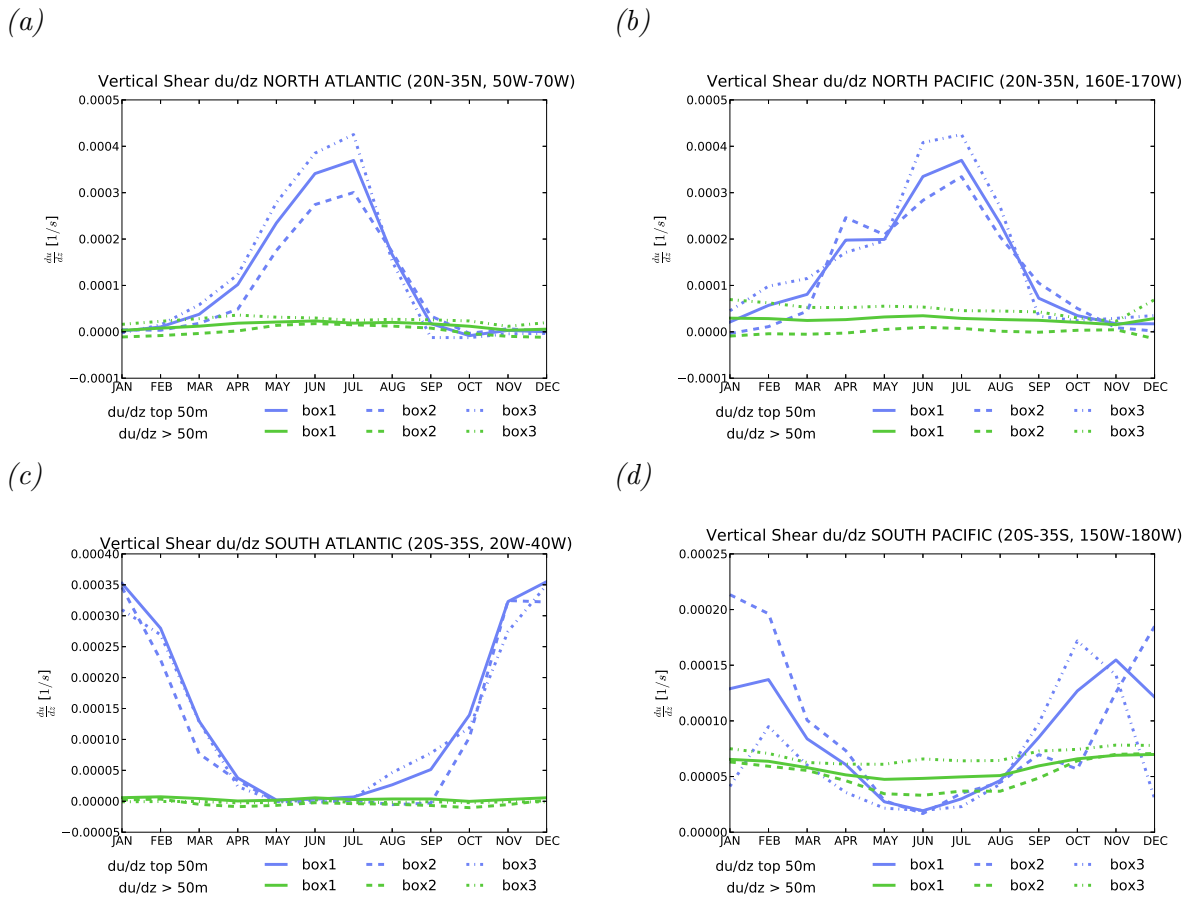

Figure 22: Vertical shear of velocity averaged over the top 50m (blue) and from 50m-500m (green). Averaged over the different boxes shown in figures 17-20 for the North Atlantic (top left), North Pacifc (top right), South Atlantic (bottom left) and South Pacific (bottom right).

deeper ocean (averaged from $50m - 500m$), however, exhibits no significant vertical shear of horizontal velocities in any season. Further inspection of a selection of vertical profiles of horizontal velocity (Fig. 23 (a) and (b)) shows the observed vertical shear to be located at the base of the Mixed Layer. In the NA (Fig. 23 (a)), in January, no vertical shear of horizontal velocity is observed in the top $70m$ with $U \sim 2.2cms^{-1}$. Beneath the Mixed Layer a weak shear is observed when U increases towards $2.4cm^{-1}$ at $140m$. The velocity profile further down is very similar in all seasons. In July, a large shear is observed near the surface. Velocities of $4cms^{-1}$ in the very shallow Mixed Layer decrease towards the background flow in the main thermocline. In October, the Mixed Layer depth increases to $\sim 30m$, as can be concluded from the homogeneous U above and the shear towards the

background around $50m - 70m$ depth. In the NP (Fig. 23 (b)) the evolution of horizontal velocity throughout the year is similar. A rather constant background flow below $200m$ is opposed by strongly variable flow close to the surface. Generally the velocities are slightly larger in the NP, compared to the NA. In July, a maximum velocity of almost $5cms^{-1}$ is observed in the very shallow Mixed Layer, leading to a large shear towards the layers below. Also, in January, the shear is highest at the base of the Mixed Layer at around $120m$.

In the SH, the SA's seasonal cycle of vertical shear of U (Fig. 22 (c)) is comparable to the cycles observed in the NH. Maximal shear between $0.3 \times 10^{-3} s^{-1}$ and $0.4 \times 10^{-3} s^{-1}$ is reached in the summer months (November to February) and negligible vertical shear is observed in winter (May to July), as well as below the Mixed Layer, averaged from

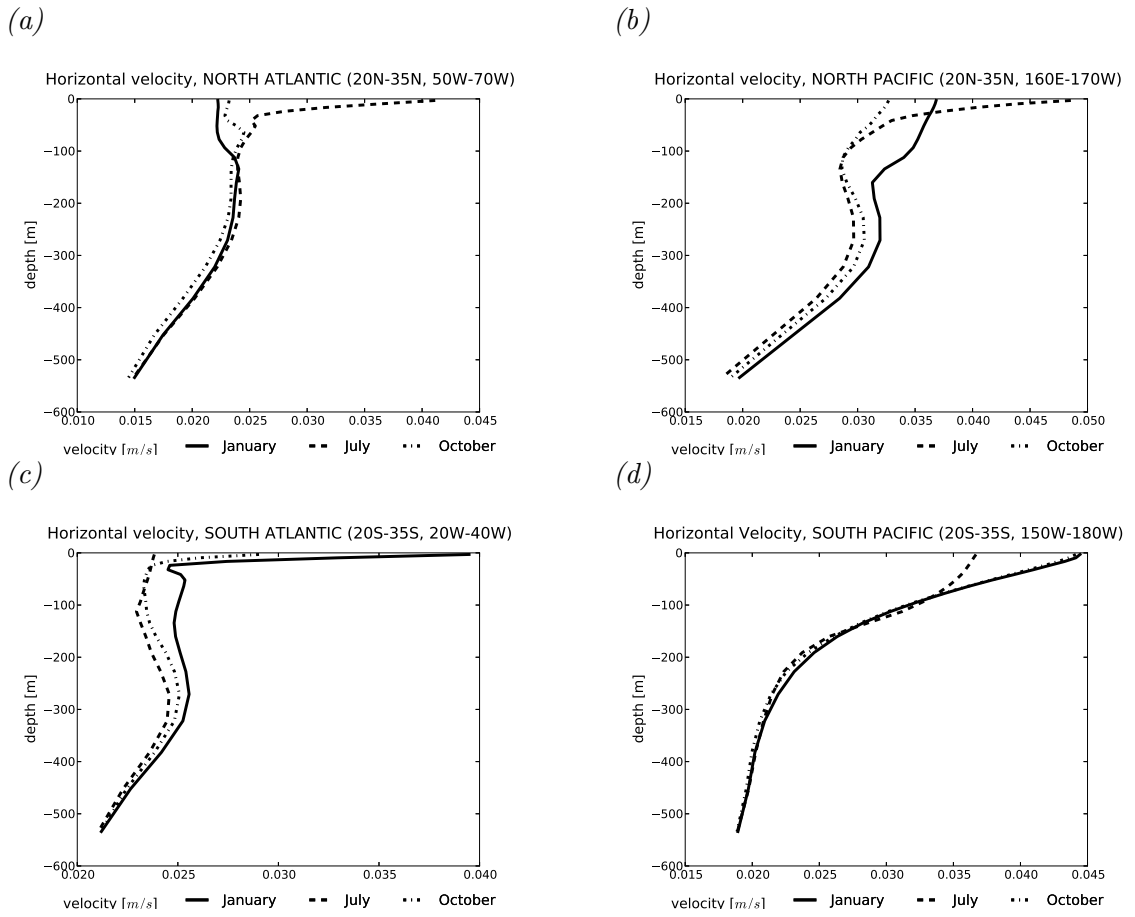

Figure 23: Profiles of velocity $|U|$ for January (solid), July (dashed) and October (dash-dotted). Averaged over the boxes (1) shown in figures 17-20 for the North Atlantic (top left), North Pacifc (top right), South Atlantic (bottom left) and South Pacific (bottom right).

$50m - 500m$. The profiles of horizontal velocity (Fig. 23 (c)) are also comparable to the NH counterparts. When the Mixed Layer is shallow in January, velocities at the surface are strong ($4cms^{-1}$) and in winter velocities are small ($< 2.5cms^{-1}$) everywhere. Contrary to the other three investigated gyres, the SP has an overall lower level of vertical shear with maxima around $0.2 \times 10^{-3}s^{-1}$ (Fig. 22 (d)). While box SP(2) of the SP exhibits the known pattern of maximum shear in summer in the top $50m$ and almost no shear in winter and below $50m$, box SP(3) shows a different behaviour. The vertical shear of the top $50m$ in box SP(3) has a maximum in October followed by a minimum in December, with a secondary maximum in February. Throughout the winter months, the annual cycle in box SP(3) is similar to that of box SP(2). The profiles of $|U|$ in the SP (Fig. 23 (d)) also are significantly different from the other three gyres. An almost constant decrease of $|U|$ from the surface down to $200m$ is observed in the summer months (October and July) and the surface velocity is only slightly decreased in winter (July).

The investigated vertical shear of horizontal velocity (Fig. 22) and vertical profiles of this velocity (Fig. 23) suggest surface-intensified mechanisms being responsible for the annual cycle of surface EKE. This suggestion is supported by an inspection of EKE at $100m$ depth (Fig. 24) and vertical profiles of EKE (Fig. 25). The EKE at $100m$ depth and the profiles of EKE have been derived from a second model run, from which data at depth was available, but investigations of EKE profiles are assumed to be transferable to the results from the main run (cf. section 2.2).

The EKE at $100m$ generally shows significantly reduced or absent seasonal cycles compared to the surface. In the NA (Fig. 24 (a)), the southern part of the investigated region (box NA(2)) has no annual cycle at all with EKE $\sim 20cm^2s^{-2}$ throughout the year. The northern box NA(3) shows a minimum in EKE ($\sim 31cm^2s^{-2}$) from February to April but no summer maximum as EKE levels remain around $37cm^2s^{-2}$ from June to December. Most notable concerning the surface intensification of the seasonal cycle, in winter, EKE at $100m$ is only reduced by $< 5cm^2s^{-2}$ and $< 10cm^2s^{-2}$ for box NA(3) and NA(2), respectively, while the reduction compared to the surface exceeds $20cm^2s^{-2}$ in summer. A similar pattern is observed in the NP (Fig. 24 (b)). Mean EKE is higher in the NP than in the NA as already noticed before (Fig. 17 and 18) and the annual cycle

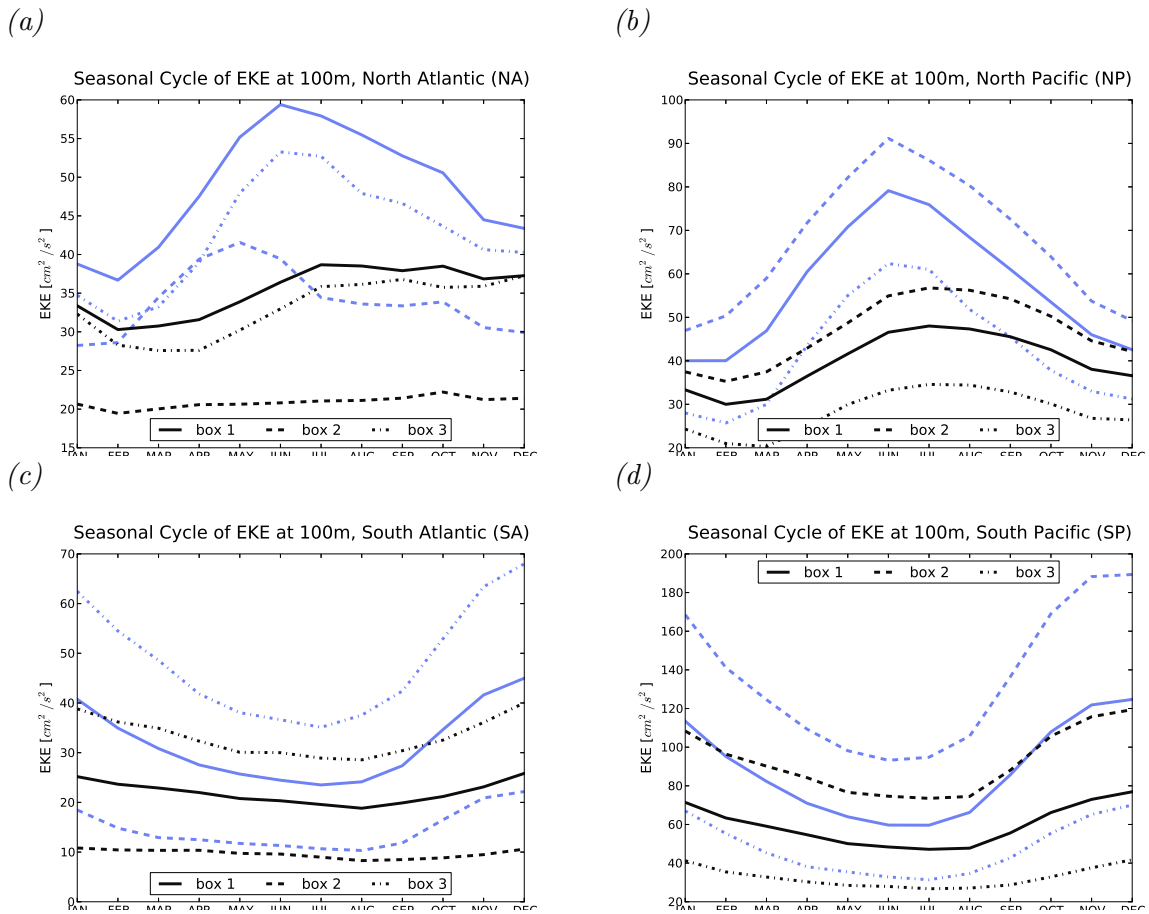

Figure 24: EKE at $100m$ *depth (black lines) from a second model run and surface EKE (blue) from the same model run for comparison. Averaged over the different boxes shown in figures 17-20 for the North Atlantic (top left), North Pacifc (top right), South Atlantic (bottom left) and South Pacific (bottom right).*

is more pronounced. In contrast to the NA, the summer maximum is detectable at $100m$ depth in the NP in all boxes. Similar to the NA though, the reduction of EKE compared to the surface is much larger in summer ($\sim 30cm^2s^{-2}$) compared to winter ($10cm^2s^{-2}$ in box NP(2), $5cm^2s^{-2}$ in box NP(3)). Additionally, there is a shift in the phase of the seasonal cycle. At the surface, the maximum EKE in the NP is located in June, while at $100m$ depth, the seasonal cycle peaks in July/August. The SA EKE at $100m$ depth (Fig. 24 (c)) is comparable to the NA. The area closer to the equator (box SA(2)) has no annual cycle, while box SA(3) has a weak seasonal cycle at $100m$. As in the NA, the EKE at $100m$ is only marginally decreased compared to the surface EKE in winter, but shows a significant reduction of $> 40\%$ in summer. As in the NH, the EKE in the SP

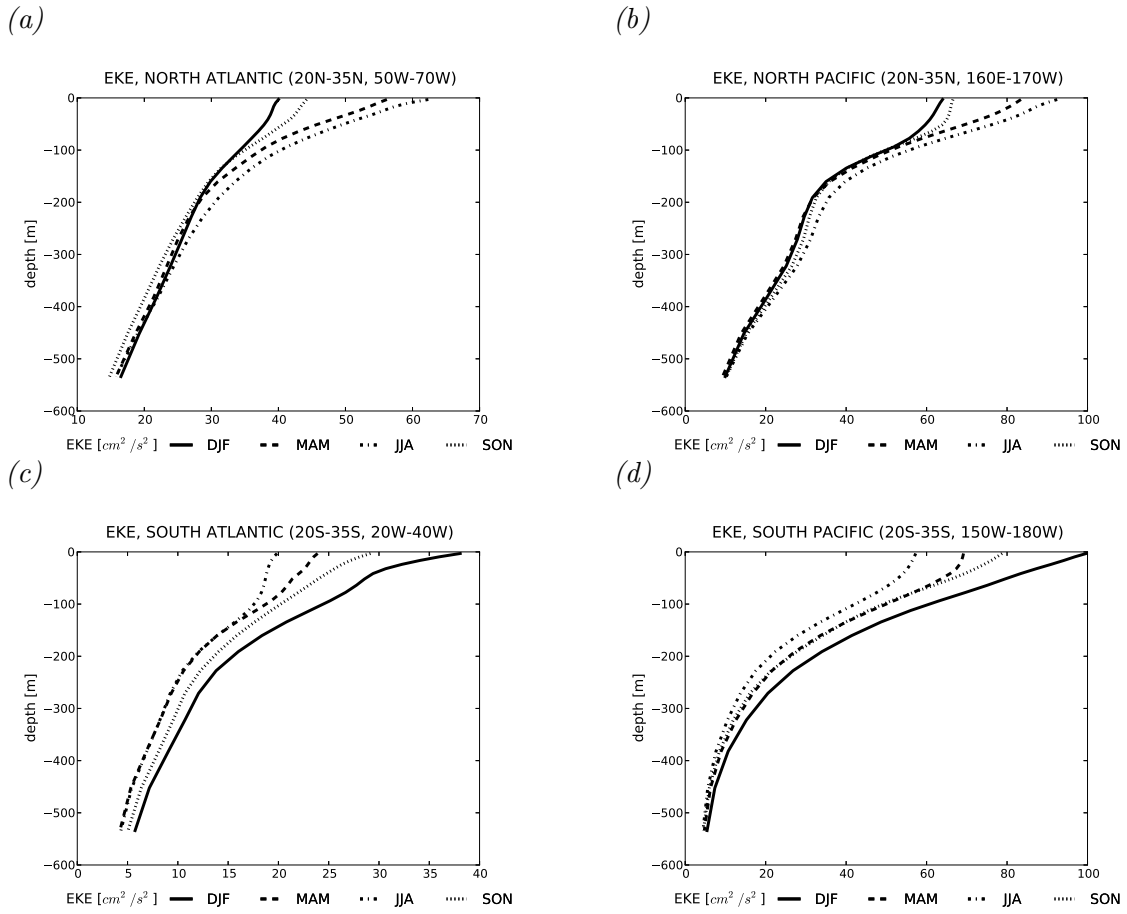

Figure 25: Profiles of EKE from the surface to $\sim 500m$ for winter (DJF, solid), spring (MAM, dashed), summer (JJA, dash-dotted) and fall (SON, dotted). Averaged over boxes (1) shown in figures 17-20 for the North Atlantic (top left), North Pacifc (top right), South Atlantic (bottom left) and South Pacific (bottom right). EKE here is only a 2-year average.

(Fig. 24 (d)) is larger than in the Atlantic in the mean but the evolution of EKE at $100m$ depth is similar to the other three subtropical gyres with small reductions compared to the surface in winter and substantial decrease of EKE towards depth in summer.

To further illustrate the above mentioned decrease of the seasonal cycle's amplitude, figure 25 depicts vertical profiles of EKE for the four investigated subtropical gyres. The monthly EKE used here is only a two-year mean 'climatology' ,in contrast to the 26 years used in the rest of the study. Though, as the interannual variability in the subtropical gyres is low (Fig. 17-20), the presented results are assumed to represent the mean state to a satisfying extend.

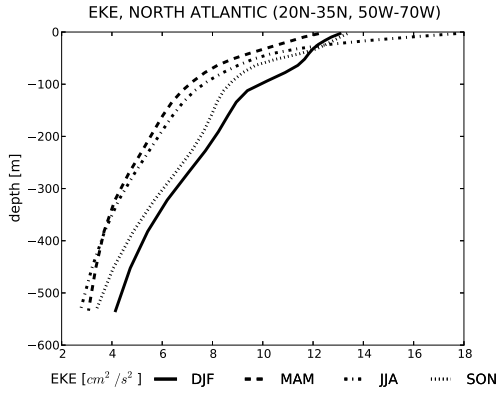

Figure 26: as Fig. 25 (a) but for EKE from a 1/4° model.

The vertical profiles of EKE in the NA (Fig. 25 (a)) and NP (Fig. 25 (b)) are similar. EKE is $\sim 15cm^2s^{-2}$ at $500m$ depth, increasing to $\sim 30cm^2s^{-2}$ at $200m$. Closer to the surface the NP exhibits a stronger increase than the NA, with surface EKE between $60cm^2s^{-2}$ and $100cm^2s^{-2}$ in the NP and $40cm^2s^{-2} - 60cm^2s^{-2}$ in the NA. The Pacific's higher mean surface EKE is shown in section 4.3. A shared property of both NH subtropical gyres is the absence of significant seasonal variations of EKE below $200m$ depth. In the NP, homogeneous EKE throughout the year extends up to $100m$. Above this low variability at depth, a seasonal cycle can be observed, which drastically increases towards the surface, resulting in the maximum amplitude of the annual cycle of EKE at the sea surface. The profiles of EKE in the SA (Fig. 25 (c)) compare well to the NA. A surface intensified annual cycle is found above $\sim 120m$, on top of an ocean interior with weak seasonal variability. Concerning the vertical distribution of EKE, the SP is a special case compared to the other three subtropical gyres investigated, as already seen in figure 23. Although the annual cycle of EKE is surface intensified in the SP, as in the other gyres, a weak seasonal cycle can also be found at depth (down to $\sim 300m$). Near the surface however, the SP is almost identical to the NP with a clear EKE maximum in summer and lowest EKE in winter.

With 1/12° resolution the ORCA12 model is able to produce variability on the sub-mesoscale with length-scales of only a few kilometers. To rule out the possibility of sub-mesoscale variability being responsible for the observed surface intensification of variability, a similar profile of EKE is derived from the ORCA025 1/4° model (Fig. 26). The ORCA025 model is based on the same model code as ORCA12 but differs in resolution and some parametrizations. Nevertheless, the profiles of EKE, exemplarily shown for the NA region, show the surface-intensification in fact to be a property of the mesoscale kinetic energy, especially emphasized in the summer months.

Summarizing the results of section 5.1.2, it is evident, that the seasonal cycle of the vertical shear of horizontal velocity is strongly correlated to the seasonal cycle of surface EKE in the subtropical gyres. Although this correlation does not prove any causalities, there are several facts that point towards some form of connection between this vertical shear and the EKE.

Previous studies already found the weak mean currents of the mid-ocean to be able to generate EKE through baroclinic instability (Arbic, 2000; Gill et al., 1974) and more important, Beckmann et al. (1994) indeed pointed out the importance of a velocity shear between the Mixed Layer and the interior ocean, especially in the subtropical gyres. A study by Yang et al. (2013), based on ARGO floats in the northwestern Pacific found cyclonic and anticyclonic eddies to be trapped near the surface, only extending downwards to $120m$ and $100m$, respectively, in a region comparable to the NP region of this study. Furthermore, a remote source of the seasonal cycle of observed EKE in the mid-ocean is unlikely, as the whole subtropical gyres exhibit the same phase of the annual cycle. If EKE propagated to the interior of the gyres from strongly unstable boundary currents, a phase shift with distance from these currents could be expected (as observed in the South Indian Ocean subtropics, where the Leeuwin Current west of Australia radiates EKE into the subtropical gyre (Scharffenberg and Stammer, 2010)). Taking into account the surface-intensified seasonal cycle of EKE described in this section, one hypothesis seems favourable to explain the source of this cycle in the subtropical gyres: A background field of EKE without a seasonal cycle exists in the gyres' interior, the source of which cannot be identified within the limits of this study. Superimposed onto this background EKE, the local near-surface shear generates additional EKE in summer which is responsible for the observed seasonal cycle. Nevertheless, a combination of the external atmospheric dissipation processes and some internal generation mechanisms cannot be ruled out as a source for the seasonal cycle in EKE. Additionally, some factors not accounted for in this study could also play a role.

5.2 The Western Boundary Currents and Interannual Variability

In the WBC regions, the discussion focusses on the two dissipation processes presumably involved in producing the seasonal cycle of surface EKE. Baroclinic and barotropic instability processes are well known to be the source of EKE in these regions and do not exhibit a strong seasonal cycle or maximum in winter (Zhai et al., 2008). Investigating the vertical shear of horizontal velocities will not at all account for the various different EKE generation mechanisms here, so an inspection of these terms will not be undertaken.

The annual cycles of the density difference between $160m$ depth and the surface in the GS and Kuroshio current systems (Fig. 27) both show a low level of stratification from December to April, then increasing towards a maximum in August and August/September in the GS and Kuroshio, respectively. The wind stress is generally higher in the vicinity of the WBCs, compared to the interior subtropical gyres (Fig. 24). Furthermore a clear seasonal cycle can be observed in both, the GS and Kuroshio current systems, with largest wind stress $> 0.15 Nm^{-2}$ in winter (maxima $\sim 0.18 Nm^{-2}$ in January). In the GS, as well as in the Kuroshio region, wind stress exhibits a gradual decline from February to May after the winter maximum, followed by reduced wind stress ($\sim 0.06 Nm^{-2}$) throughout the summer until September in the GS and October

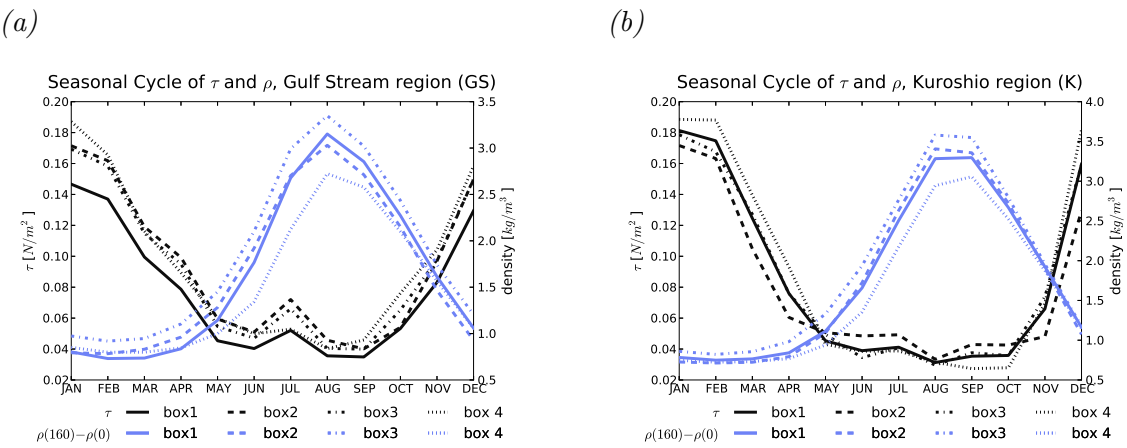

Figure 27: Mean seasonal cycles for the density difference between 160m depth and the surface (blue) as an indicator of the strength of the stratification and the wind stress (black). Averaged over different boxes shown in figure 13 for the Gulf Stream region (left) and Kuroshio region (right).

in the Kuroshio region. The wind stress is therefore three to four times higher in winter, compared to summer. Although the seasonal cycles of the two inspected dissipation mechanisms seem to favour the hypothesis of dissipation being responsible for the observed annual cycle in surface EKE, there still are some discrepancies that hint to some other factors being involved. First, while wind stress is at approximately the same, low level from May to October and stratification has its maximum in August/September, the maximum in surface EKE is observed in June/July. This feature cannot be explained directly by either of the dissipation terms or a combination of both. Second, while in the annual cycle of surface EKE a shift of the phase towards later in the year is observed towards the east (downstream), there is no such shift in the dissipation terms. Despite having a clear and substantial influence on the seasonal cycle of surface EKE, the dissipation through wind work and heat fluxes does not succeed in explaining it in detail. It is assumed, that other processes, such as the advection of EKE with the mean current, should not be neglected in the WBC systems.

As for the subtropical gyres, the EKE at $100m$ depth from a second model run (cf. section 2.2) is compared to the surface EKE (Fig. 28) to test for possible surface intensification of the seasonal cycle. In the GS region (Fig. 28 (a)), especially when averaged over the whole area (box GS(1)), the seasonal cycle present at the surface is

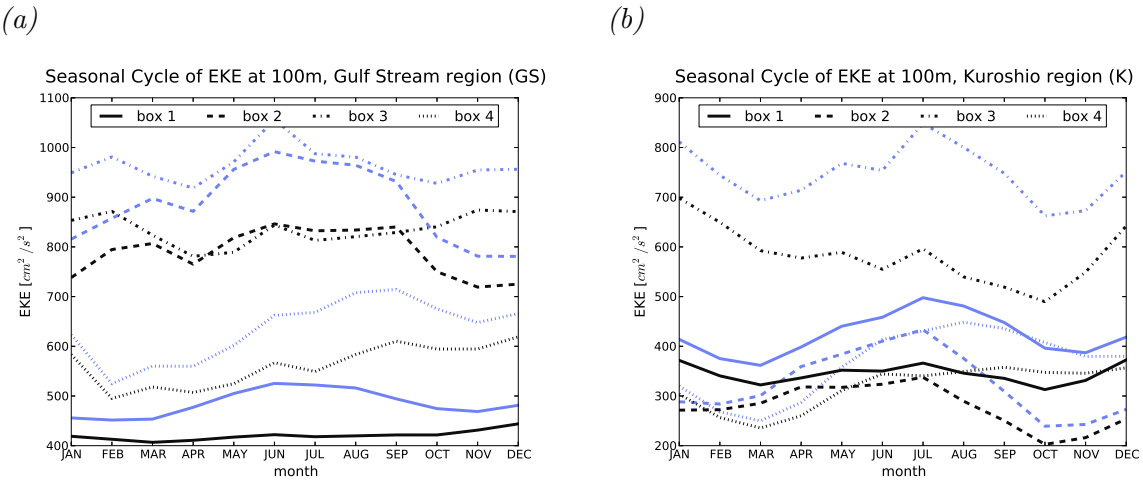

Figure 28: EKE at $100m$ *depth (black lines) from a second model run and surface EKE (blue) from the same model run for comparison. Averaged over the different boxes shown in figure 13 for the Gulf Stream region (top left) and the Kuroshio region (right)*

absent at $100m$ depth with only a weak maximum in December. Also for boxes GS(3) and GS(4) the maximum surface EKE in summer/late summer is not detectable at $100m$. Only in box GS(2) does the EKE at $100m$ peak in the summer months. Notably, the difference of EKE at the surface to EKE at $100m$ is larger in summer compared to winter. This difference is up to $200cm^2s^{-2}$ in boxes GS(2) and GS(3) and $100cm^2s^{-2}$ in boxes GS(1) and GS(4) in summer and only $< 100cm^2s^{-2}$ in boxes GS(2) and GS(3) and $< 50cm^2s^{-2}$ in boxes GS(1) and GS(4) in winter. This compares well to the annual cycle of EKE at $100m$ depth in the Kuroshio region (Fig. 28 (b)). Similar to the GS, box K(1) shows no annual cycle at $100m$ depth with differences to the surface being up to ~ 4 times higher in summer, compared to winter. Averaged over box K(3), the seasonal cycle even exhibits a clear maximum in winter at $100m$, opposed to a maximum in July at the surface. Boxes K(2) and K(4) have no phase shift at $100m$ compared to the surface but still show greater reduction of EKE at depth in summer, compared to winter.

The reduction, or in some cases reversion, of the annual cycles of EKE at $100m$ depth, compared to the surface EKE, indicates surface or near-surface processes to be responsible for the observed seasonal cycle at the surface. This supports the hypothesis of wind work and thermal dissipation being the driving factors in determining seasonal variability of surface EKE in the vicinity of the WBCs, as these factors are atmospherically driven and therefore clearly surface-related.

(a) *(b)*

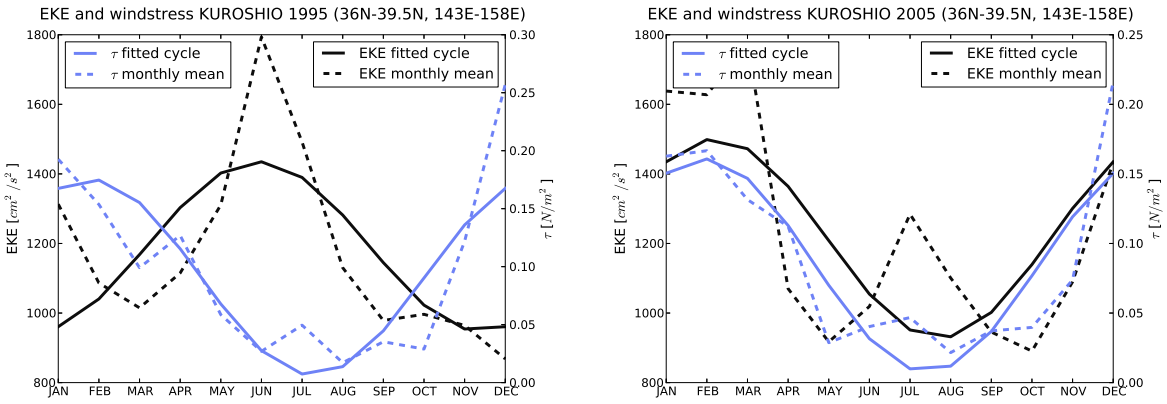

Figure 29: Wind stress τ (blue) and surface EKE (black) in the Kuroshio region for 1995 (left) and 2005 (right. Dashed lines indicate the monthly mean values, solid lines show the fitted seasonal cycle.

Although, averaged over the available 26 years, the dissipation of surface EKE seems to be the driving mechanism in determining the annual cycle, the generation of EKE in the WBCs remains a highly chaotic process and the presented results cannot be transferred to an analysis of single years. On a yearly basis, in some years the annual cycle of surface EKE is anti-correlated to e.g. wind stress, as expected, while in other years, the seasonal cycle of EKE is in phase with that of the wind stress. Figure 29 exemplarily shows two different years (1995 (a) and 2005 (b)) from the Kuroshio region. In 1995, the surface EKE is similar to the time-mean seasonal cycle (Fig. 16) with a summer maximum and low levels of EKE during the winter, when the wind stress is large. Contrary, in 2005 the annual cycles of wind stress and EKE are in phase. Although the seasonal cycle of wind stress is almost identical to the one in 1995, the surface EKE does not respond to this cycle, showing maximal EKE in winter and low EKE in summer. This illustrates the complexity of generation and dissipation mechanisms for EKE and emphasizes the need of long time series to produce robust results when studying EKE, especially in highly energetic regions. Additionally, figure 29 shows that the presented results should not be transferred to isolated events or periods.

6 Summary and Conclusion

Using the ORCA12 global ocean model with a resolution of 1/12°, the aim of this thesis was to study the temporal variability, especially the seasonal cycle, of surface Eddy Kinetic Energy.

First, the reference period to which the deviations from the mean horizontal velocities $\overline{u}$ and $\overline{v}$ should be calculated was discussed. It was shown, that the choice of the whole available time span as a reference period leads to an overestimation of EKE (Fig. 1), as variations of u and v on internannual time scales are regarded as deviations from the mean. As the EKE is the mesoscale variability with time scales of weeks to months, this needs to be avoided. Further investigations showed a reference to yearly mean $\overline{u}$ and $\overline{v}$ to be sufficient. This still includes possible contributions of seasonal cycles of u and v to the EKE, but these influences seem to be negligible (Fig. 2). Additionally, a distinction

of mesoscale variability with time scales of a few months from a mean seasonal cycle in u and v is not possible, so one year mean $\overline{u}$ and $\overline{v}$ are favourable.

Also in section 3, it has been proven that, while the differences between the surface EKE calculated from geostrophic currents and the total surface EKE are considerably large (up to $\sim 100 cm^2 s^{-2}$) in high energy regions such as the GS, Kuroshio, ACC etc. (Fig. 3), the annual cycle is not influenced significantly (Fig. 4). It is therefore reasonable to compare seasonal cycles derived from geostrophic velocities (e.g. from satellite altimetry) to total surface EKE from the model.

Comparison of the ORCA12 model output with AVISO satellite altimetry data revealed, it is not only methodologically reasonable to compare them but indeed the model reproduces the observed mesoscale variability. Both, the SSH variance (Fig. 5 and 6) and the mean EKE (Fig. 7 and 8), are similar in major parts of the Atlantic and Pacific Oceans. Regional differences include the displacement of the separation points of the NH WBCs by roughly 2° to the north in ORCA12 compared to AVISO. Additionally, extrema are not as pronounced in ORCA12, while the regions with medium EKE levels are comparable between ORCA12 and AVISO. Crucial for the further discussion about the temporal variability of EKE, the amplitude and phase of the mean seasonal cycle of surface EKE in AVISO and ORCA12 show great agreement. As the mean EKE, the amplitude of the seasonal cycle (Fig. 9 and 10) is slightly too low in high energy regions but ORCA12 has an intriguingly good representation of the phase of the seasonal cycle in all regions of interest here (Fig. 11 and 12). Both hemisphere's subtropical gyres have a maximum EKE in the summer months with slight modifications depending on the exact latitude. Furthermore, regions showing no significant seasonal cycle in ORCA12 coincide with regions exhibiting a spatially inhomogeneous distribution of the phase of the seasonal cycle in AVISO. Based on the amplitudes and the spatial homogeneity of the seasonal cycle, six regions where chosen for detailed investigations: The Gulf Stream and Kuroshio regions with their high EKE levels and the adjacent regions in the western interior of the NH subtropical gyres of the Atlantic and Pacific and their SH counterparts.

The most energetic areas in the GS and Kuroshio are located in the western parts (Fig. 13), close to their separation points, with mean EKE $> 2000 cm^2 s^{-2}$ and amplitudes

of the seasonal cycle $> 500cm^2s^{-2}$. The eastward extend of mean EKE levels between $500cm^2s^{-2}$ and $1000cm^2s^{-2}$ and amplitudes $> 100cm^2s^{-2}$ is $40°W$ in the GS and $175°E$ in the Kuroshio. Concerning the phase of the seasonal cycle, the WBCs have some very local, distinct features separating them from the surrounding regions. Coinciding with mean EKE levels $> 1000cm^2s^{-2}$ near the axis of the GS and Kuroshio systems, a maximum of the seasonal cycle in winter/spring is evident, with spring maxima to the south and a gradual shift to winter maxima towards the north (Fig. 13 and 14). Averaged over the region though, these maxima are associated with small amplitudes relative to the mean EKE and the interannual variability of the seasonal cycle is large, especially in the Kuroshio (Fig. 16). Although a bias from calculating EKE with respect to yearly mean u and v could be ruled out as the source for an altered seasonal cycle of EKE in the Gulf Stream region in general in section 3, in such localized features, the seasonal cycle of u and v could be misinterpreted as EKE. Additionally, a meridional shift of the WBCs with the seasons could lead to such a seasonal cycle. Another possible solution for this small regional spring/winter maximum in EKE is the EKE generation peaking in winter. Zhai et al. (2008) estimate the EKE production to be highest in winter in the GS and explain the general summer phase with energy dissipation also being largest in winter. In the core regions of the WBCs however, EKE production in winter could be very large with the effect of dissipation not being sufficient to impose its seasonal cycle. While away from the cores of the WBCs, the dissipation, especially through wind stress, is similar and the EKE production is significantly smaller, allowing the dissipation to be the driving factor in the seasonal cycle. Thus, outside these most energetic core regions the maximum of the seasonal cycle is located in the summer months in the vicinity of the WBCs, with a small shift towards September downstream.

Just adjacent to the WBC regions, the NH western interior subtropical gyres also exhibit maximal surface EKE in summer (Jun.-Aug.). The spatial distribution of the phase of the seasonal cycle in these regions is rather homogeneous and very similar between Atlantic (Fig. 17 and 19) and Pacific (Fig. 18 and 20), even though the two regions show different dynamical settings. In the NP the Subtropical Counter Current lies within the inspected region, while in the NA no such current band is present. Generally, the

mean EKE in the NA and NP ranges between $30cm^2s^{-2}$ and $100cm^2s^{-2}$ with amplitudes of the seasonal cycle of the same magnitude in the NP and $5cm^2s^{-2} - 30cm^2s^{-2}$ in the NA.

The SA and SP exhibit similar behaviour. Mean EKE in the SA is $10cm^2s^{-2} - 50cm^2s^{-2}$ and in the SP $10cm^2s^{-2} - 100cm^2s^{-2}$ with an equatorward band of high EKE, as in the NP. The seasonal cycle in the SH also exhibits strong similarity to the NH with amplitudes slightly higher in the Pacific compared to the Atlantic and a general summer maximum (Nov.-Feb.).

After evaluating the model's performance and describing the seasonal cycles of surface EKE in the several regions, three mechanisms were tested for their probability of being the source of seasonal variability of EKE. Two of these mechanisms focus on dissipation processes acting upon the EKE at the sea surface. During the winter months, large heat fluxes from the ocean to the atmosphere, especially in the WBC regions, dissipate EKE in the surface Mixed Layer, while the seasonal thermocline with a very strong stratification near the surface decouples the EKE from atmospheric forcing in summer (Zhai and Greatbatch, 2006b). To assess this mechanism, the difference of potential density between $160m$ depth and the surface was used as an indicator for the strength of the stratification and therefore the decoupling of EKE from the atmosphere. The other possible dissipation mechanism is the wind work. As wind speeds at midlatitudes are much larger in winter compared to summer, the effect of wind and the associated wind stress and work on the ocean is larger in winter as well. Furthermore, wind work acts as a damping on EKE. This damping is introduced by effects of the relative velocity between the atmospheric winds and oceanic currents (Zhai and Greatbatch, 2007). The possible effect of wind stress on EKE was tested by inspection of the annual cycles of wind stress. The third proposed mechanism is not a dissipation process, but a generation process located in the near-surface ocean. Local instabilities caused by a vertical shear of horizontal velocities at the base of the Mixed Layer are thought to generate surface-intensified EKE (Beckmann et al., 1994). The role of this shear instabilities in producing a seasonal cycle in surface EKE was tested by investigations of the vertical shear of velocities and the vertical structure of EKE in the top $500m$ of the water column.

In the WBC regions, the hypothesis of dissipation mechanisms being responsible for the observed seasonal variations in surface EKE (Zhai et al., 2008) can be supported. In both regions, the GS and the Kuroshio, wind stress peaks in the winter months with considerable strength of up to $0.2Nm^{-2}$, accompanied by a weak stratification (Fig. 26). A combination of wind work and thermal dissipation results in a significant damping of surface EKE in winter, leading to enhanced EKE levels in the summer months. This was supported by an investigation of the annual cycle of EKE at $100m$ depth, showing reduced or absent seasonal variations of EKE, compared to the surface (Fig. 28). In the WBCs, the generation of EKE exhibits only a weak maximum in winter (Zhai et al., 2008) which should result in almost constant surface EKE throughout the year. This seasonally constant EKE is then altered in the near-surface layers by dissipation processes originating in the overlying atmosphere. Nevertheless, in the chaotic WBC regimes, the actual balance of EKE generation and dissipation varies largely from year to year, resulting in differing seasonal cycles (Fig. 29). Only averaged over a sufficiently long period, the above mentioned processes are able to explain the observed seasonal cycle. An investigation of the vertical shear of velocities in the WBCs has not been undertaken in this study as this simplified view could not account for the various processes of baroclinic and barotropic instabilities responsible for EKE production in these regions.

In the subtropical gyres, the seasonal cycles of wind stress vary greatly between different regions. While in some areas of the gyres (e.g. the northern parts of the NH subtropical gyres), the phase of the seasonal cycle of wind stress is suitable to explain the annual variations in EKE through the proposed process, in other areas there is no annual cycle in wind stress or the wind stress is in phase with the annual cycle of surface EKE (Fig. 21). The surface EKE however peaks in summer everywhere, leading to the conclusion that the dissipation through wind stress cannot generally explain the seasonal cycle of EKE in the subtropical gyres. Additionally, it has to be kept in mind that the wind stress is much weaker in the subtropics compared to the midlatitude WBC regions, reducing the possible impact on EKE. The same holds for damping through thermal interactions with the atmosphere. Surface intensified changes in EKE can be induced by variations in the dissipation time scales in the Southern Ocean (Zhai and Munday,

2014). In the subtropics however, while the seasonal cycle of the stratification is roughly in agreement with the cycle needed to explain the proposed damping process, the heat fluxes from the ocean to the atmosphere could be too small to sufficiently decrease surface EKE. A further, more detailed investigation of heat fluxes and associated dissipation in the subtropical gyres is needed to confirm this, though.

The suitability of the two proposed dissipation mechanisms to explain the observed annual cycle of surface EKE in the subtropical gyres is questionable. Therefore, a third hypothesis was tested. Baroclinic instability at the base of the Mixed Layer is thought to locally generate EKE in the subtropical gyres (Beckmann et al., 1994). To support this hypothesis, the annual cycle of vertical shear of horizontal velocity and profiles of this velocity as well as EKE were investigated. The vertical shear of the mean flow was found to have no significant seasonal cycle below $50m$ depth (Fig. 22). In the top $50m$ of the water column however, the vertical shear exhibits a strong seasonal cycle that peaks in summer in all investigated regions. As this annual cycle of vertical shear is in phase with the seasonal variations of surface EKE, some form of connection can be assumed. A detailed inspection of vertical profiles of horizontal velocity (Fig. 23) revealed, that the location of the largest vertical shear is indeed correlated to the depth of the base of the Mixed Layer. In summer, the maximal shear is found in the surface layers, whereas in winter it is located between $100m$ and $200m$ depth. Comparing these profiles of velocity with profiles of EKE (Fig. 25) further showed the EKE also to be surface intensified, with absent seasonal variations below $300m$, but drastically increasing variability towards the surface. Therefore, it is likely that the vertical shear found near-surface in summer makes the flow unstable, generating EKE. In the winter months though, there is no substantial vertical shear found in the entire water column. Thus, a background EKE field present in the subtropical gyres seems probable. Superimposed on this background field, there is local production of EKE through baroclinic instabilities associated with the Mixed Layer in summer. Although this hypothesis seems reasonable, it is also possible that some factors not accounted for in this study or some processes not yet understood play a role in determining the seasonal cycle of EKE in the subtropical gyres. Furthermore, for the subtropical gyres, this hypothesis could only explain the seasonal cycle of near-

surface EKE. The source of EKE in general remains unknown and with surface processes determining the surface EKE in both, the WBCs and the subtropical gyres, will remain hard to determine. One possibility is, that EKE is generated in rather strong currents with no seasonal variations and then radiates into the rest of the basin. In the WBCs the wind stress and thermal capping then determines the seasonal cycle, while in the interior of the gyres locally generated near-surface EKE is the source of the annual variations of surface EKE. On the other hand, the source of EKE at depth could be local instability almost everywhere (Arbic, 2000).

It becomes clear, while supporting some hypotheses previously made by other authors, this study cannot give clear answers to many of the questions stated at the beginning. One of the most important findings is the ability of the model to successfully reproduce the distribution of surface EKE and its seasonal variations in great detail. Based on this result, many investigations focussed on various aspects of this study can be planned and conducted in the future. The different dissipation mechanisms should be tested in greater detail with specially designed model runs. A model run with no seasonal variations in the wind field for example could determine the effect of the wind stress on surface EKE. The same could be done for the thermal interactions with the atmosphere. In the current model, the heat fluxes are based on bulk formulae not accounting for the actual ocean temperatures. Implementing heat fluxes which consider the feedback of ocean temperature onto the atmosphere could be used and altered to inspect the resulting variations in EKE. Another crucial point to be focussed on in future research is the vertical shear associated with the Mixed Layer. A more robust inspection of the vertical profiles of velocities should be undertaken in order to determine vertical shear modes found in the subtropical gyres and test them for stability.

Additionally to these more detailed persuasion of the aims of this study, the same or similar investigations should also be conducted for other regions, extended to the deep ocean or focussed on other time scales to gain better insight into the generation, dissipation and modulation of EKE.

Bibliography

Adamec, D. (1998). Modulation of the seasonal signal of the Kuroshio Extension during 1994 from satellite data. *Journal of Geophysical Research*, 103, No. C5. 10209-10222.

Arbic, B. K. (2000). *Generation of Mid-Ocean Eddies: The Local Baroclinic Instability Hypothesis*. PhD thesis, Massachusetts Institute of Technology and Woods Hole Oceanographic Institution.

AVISO (02.08.2014). http://www.aviso.altimetry.fr/en/missions.html.

Barnier, B., Madec, G., Penduff, T., Molines, J.-M., Treguier, A.-M., Le Sommer, J., Beckmann, A., Biastoch, A., Böning, C., Dengg, J., Derval, C., Durand, E., Gulev, S., Remy, E., Talandier, C., Theetten, S., Maltrud, M., McClean, J., and De Cuevas, B. (2006). Impact of partial steps and momentum advection schemes in a global ocean circulation model at eddy permitting resolution. *Ocean Dynamics*, 56, no. 5-6. 543-567.

Beckmann, A., Böning, C. W., Brügge, B., and Stammer, D. (1994). On the generation and role of eddy variability in the central North Atlantic Ocean. *Journal of Geophysical Research*, 99. No. C10, 20381-20391.

Blanke, B. and Delecluse, P. (1993). Variability of the Tropical Atlantic Ocean Simulated by a General Circulation Model with Two Different Mixed-Layer Physics. *Journal of Physical Oceanography*, 23. 1363-1388.

Brachet, S., Le Traon, P. Y., and Le Provost, C. (2004). Mesoscale variability from a high-resolution model and from altimeter data in the North Atlantic Ocean. *Journal of Geophysical Research*, 109. C12025, doi:10.1029/2004JC002360.

Cox, M. D. (1985). An Eddy Resolving Numerical Model of the Ventilated Thermocline. *Journal of Physical Oceanography*, 15. 1312-1324.

Dantzler, H. L., J. (1977). Potential energy maxima in the tropical and subtropical North Atlantic. *Journal of Physical Oceanography*, 7. 512-519.

Dickson, R. R., Gould, W. J., Gurbutt, P. A., and Killworth, P. D. (1982). A seasonal signal in ocean currents to abyssal depths. *Nature*, 295. 193-198.

Ducet, N. and Le Traon, P. Y. (2001). A comparison of surface eddy kinetic energy and Reynolds stresses in the Gulf Stream and the Kuroshio Current systems from merged TOPEX/Poseidon and ERS-1/2 altimetric data. *Journal of Geophysical Research*, 106, No. C8. 16603-16622.

Ducet, N., Le Traon, P. Y., and Reverdin, G. (2000). Global high-resolution mapping of ocean circulation from TOPEX/Poseidon and ERS-1 and -2. *Journal of Geophysical Research - Ocean*, 105. 19477-19498.

Fichefet, T. and Morales Maqueda, M. A. (1997). Sensitivity of a global sea ice model to the treatment of ice thermodynamics and dynamics. *Journal of Geophysical Research*, 102.

Fu, L.-L. (1983). Recent progress in the application of satellite altimetry to observing the mesoscale variability and general circulation of the oceans. *Reviews of Geophysics*, 21(8). 1657–1666.

Fukumori, I., Raghunath, R., and Fu, L.-L. (1998). Nature of global large-scale sea level variability in relation to atmospheric forcing: A modeling study. *Journal of Geophysical Research*, 103, no. C3. 5493-5512.

Gaspar, P., Grégoris, Y., and Lefevre, J.-M. (1990). A Simple Eddy Kinetic Energy Model for Simulations of the Oceanic Vertical Mixing: Tests at Station Papa and Long-Term Upper Ocean Study Site. *Journal of Geophysical Research*, 95. No. C9, 16179-16193.

Gill, A. E., Green, J. S. A., and Simmons, A. J. (1974). Energy partition in the large-scale ocean circulation and the production of mid-ocean eddies. *Deep-Sea Research*, 21. 499-528.

Griffies, S. M., Biastoch, A., Böning, C., Bryan, F., Danabasoglu, G., Chassignet, E. P., England, M. H., Gerdes, R., Haak, H., Hallberg, R. W., Hazeleger, W., Jungclaus, J., Large, W. G., Madec, G., Pirani, A., Samuels, B. L., Scheinert, M., Sen Gupta, A.,

Severijns, C. A., Simmons, H. L., Treguier, A. M., Winton, M., Yeager, S., and Yin, J. (2008). Coordinated Ocean-ice Reference Experiments (COREs). *Ocean Modelling*, 26. 1-46.

Hakinen, S. and Rhines, P. B. (2009). Shifting surface currents in the northern North Atlantic Ocean. *Journal of Geophysical Research*, 114. C04005, doi:10.1029/2008JC004883.

Holland, W. R., Harrsion, D. E., and Semtner Jr., A. J. (1983). In Robinson, A. R., editor, *Eddies in Marine Science*, chapter Eddy-Resolving Numerical Models of Large-Scale Ocean Circulation, pages 379–403. Springer-Verlag, Berlin; Heidelberg.

Holland, W. R. and Lin, L. B. (1975). On the Generation of Mesoscale Eddies and their Contribution to the Oceanic General Circulation. I. A Preliminary Numerical Experiment. *Journal of Physical Oceanography*, 5. 642-657.

Hurlburt, H. E., Wallcraft, A. J., Jr., W. J. S., Hogan, P. J., and Metzger, E. J. (1996). Dynamics of the Kuroshio/Oyashio current system using eddy-resolving models of the North Pacific Ocean. *Journal of Geophysical Research*, 101, No. C1. 941-976.

Iselin, C. O. (1936). A study of the circulation of the western North Atlantic. *Papers of Physical Oceanography and Meteorology*, 4, no. 4. 1-101.

Large, W. G. and Yeager, S. G. (2004). Diurnal to Decadal Global Forcing For Ocean and Sea-Ice Models: The Data Sets and Flux Climatologies. *Technical Note TN-460+STR*. NCAR, P.O. Box 3000 Boulder, Colorado 80307.

Le Traon, P. Y. and Morrow, R. (2001). In Fu, L.-L. and Cazenave, A., editors, *Satellite Altimetry and Earth Sciences*, chapter Ocean Currents and Eddies, pages 171–216. San Diego; London.

Le Traon, P. Y., Nadal, F., and Ducet, N. (1998). An improved mapping method of multisatellite altimeter data. *Journal of Atmospheric and Oceanic Technology*, 15. 522-534.

Madec, G. (2008). NEMO ocean engine. *Note du Pôle de modélisation*. Institut Pierre-Simon Laplace (IPSL), France, No 27, ISSN No 1288-1619.

Madec, G., Delecluse, P., Imbard, M., and Lévy, C. (1998). OPA 8.1 Ocean General Circulation Model reference manual. *Note du Pôle de modélisation*. Institut Pierre-Simon Laplace (IPSL), France, No 11, 91pp.

Maltrud, M. E. and McClean, J. L. (2005). An eddy resolving global 1/10° ocean simulation. *Ocean Modelling*, 8. 32-54, doi:10.1016/j.ocemod.2003.12.001.

MODE Group (1978). The Mid-Oceans Dynamics Experiment. *Deep-Sea Research*, 25. 859-910.

Penduff, T., Barnier, B., Dewar, W. K., and O'Brien, J. J. (2004). Dynamical Responses of the Oceanic Eddy Field to the North Atlantic Oscillation: A Model-Data Comparison. *Journal of Physical Oceanography*, 34. 2615-2629.

Qiu, B. (2002). The Kuroshio Extension System: Its Large-Scale Variability and Role in the Midlatitude Ocean-Atmosphere Interaction. *Journal of Oceanography*, 58. 57-75.

Richardson, P. L. (1983). Eddy Kinetic Energy in the North Atlantic From Surface Drifters. *Journal of Geophysical Research*, 88, no. C7. 4355-4367.

Robinson, A. R. (1983). In Robinson, A. R., editor, *Eddies in Marine Science*, chapter Overview and Summary of Eddy Science, pages 3–15. Springer-Verlag, Berlin; Heidelberg.

Robinson, A. R., Harrison, D. E., Mintz, Y., and Semtner, A. J. (1977). Eddies and the General Circulation of an Idealized Oceanic Gyre: A Wind and Thermally Driven Primitive Equation Numerical Experiment. *Journal of Physical Oceanography*, 7. 182-207.

Scharffenberg, M. G. and Stammer, D. (2010). Seasonal variations of the large-scale geostrophic flow field and eddy kinetic energy inferred from the TOPEX/Poseidon and Jason-1 tandem mission data. *Journal of Geophysical Research*, 115. C02008, doi:10.1029/2008JC005242.

Scheinert, M. (2014). Orca Nitty Gritty. in preparation.

Scheinert, M., Biastoch, A., and Böning, C. W. (2014). ORCA12-Kiel - The Global 1/12° Ocean Model. in preparation.

Semtner, A. J. and Mintz, Y. (1977). Numerical Simulation of the Gulf Stream and Mid-Ocean Eddies. *Journal of Physical Oceanography*, 7. 208-230.

Smith, R. D., Maltrud, M. E., Bryan, F. O., and Hecht, M. W. (2000). Numerical Simulation of the North Atlantic Ocean at 1/10°. *Journal of Physical Oceanography*, 30. 1532-1561.

SSALTO/DUACS (02.08.2014). http://www.aviso.oceanobs.com/duacs/.

SSALTO/DUACS (2011). *User Handbook: (M)SLA and (M)ADT Near-Real Time and Delayed Time Products*. CLS-DOS-NT-06-034 Issue 2.5, 16pp.

Stammer, D. (1997). Global Characteristics of Ocean Variability Estimated from Regional TOPEX/POSEIDON Altimeter Measurements. *Journal of Physical Oceanography*, 27. 1743-1769.

Stammer, D. and Böning, C. (1996). In Krauss, W., editor, *The Warmwatersphere of the North Atlantic Ocean*, chapter Generation and Distribution of Mesoscale Eddies in the North Atlantic Ocean, pages 159–193. Gerüder Borntraeger, Berlin; Stuttgart.

Stammer, D., Böning, C., and Dietrich, C. (2001). The role of variable wind forcing in generating eddy energy in the North Atlantic. *Progress in Oceanography*, 48. 289-311.

Stammer, D. and Wunsch, C. (1999). Temporal changes in eddy energy of the oceans. *Deep-Sea Research II*, 46. 77-108.

Swallow, J. C. (1976). Variable Currents in Mid-Ocean. *Oceanus*, 19, no. 3. 18-25.

Volkov, D. L. (2005). Interannual Variability of the Altimetry-Derived Eddy Field and Surface Circulation in the Extratropical North Atlantic Ocean in 1993-2001. *Journal of Physical Oceanography*, 35. 405-426.

White, M. A. and Heywood, K. J. (1995). Seasonal and interannual changes in the North Atlantic subpolar gyre from GEOSAT and TOPEX/POSEIDON altimetry. *Journal of Geophysical Research*, 100, no. C12. 24931-24941.

Willebrand, J., Philander, S. G. H., and Pacanowski, R. C. (1980). The Oceanic Response to Large-Scale Atmospheric Disturbances. *Journal of Physical Oceanography*, 10. 411-429.

Wyrtki, K., Magaard, L., and Haager, J. (1976). Eddy energy in the oceans. *Journal of Geophysical Research*, 81. 2641-2646.

Xu, C., Shang, X.-D., and Huang, R. X. (2011). Estimate of eddy energy generation/dissipation rate in the world ocean from altimetry data. *Ocean Dynamics*, 61. 525-541, doi:10.1007/s10236-011-0377-8.

Yang, G., Wang, F., Li, Y., and Lin, P. (2013). Mesoscale eddies in the northwestern subtropical Pacific Ocean: Statistical characteristics and three-dimensional structures. *Journal of Geophysical Research*, 118. 1906-1925, doi:10.1002/jgrc.20164.

Zhai, X. and Greatbatch, R. J. (2006a). Inferring the eddy-induced diffusivity for heat in the surface mixed layer using satellite data. *Geophysical Research Letters*, 33. L04607, doi:10.1029/2006GL027875.

Zhai, X. and Greatbatch, R. J. (2006b). Surface eddy diffusivity for heat in a model of the northwest Atlantic Ocean. *Geophysical Research Letters*, 33. L04606, doi:10.1029/2006GL028907.

Zhai, X. and Greatbatch, R. J. (2007). Wind work in a model of the northwest Atlantic Ocean. *Geophysical Research Letters*, 34. L04606, doi:10.1029/2006GL028907.

Zhai, X., Greatbatch, R. J., and Kohlmann, J.-D. (2008). On the seasonal variability of eddy kinetic energy in the Gulf Stream region. *Geophysical Research Letters*, 35. L24609, doi:10.1029/2008GL036412.

Zhai, Z. and Munday, D. R. (2014). Sensitivity of Southern Ocean overturning to wind stress changes: Role of surface restoring time scales. *Ocean Modelling*, 84. 12-25, doi:10.1016/j.ocemod.2014.09.004.

Appendix

I The Fitting Method

$$A\sin(x) + B\cos(x) + C = y$$

where $x = \dfrac{t}{12}$

$$\sqrt{A^2+B^2}\left(\frac{A}{\sqrt{A^2+B^2}}\sin(x) + \frac{B}{\sqrt{A^2+B^2}}\cos(x)\right) + C = y$$

with $\dfrac{A}{\sqrt{A^2+B^2}} = \cos(\arctan(\dfrac{B}{A}))$ and $\dfrac{B}{\sqrt{A^2+B^2}} = \sin(\arctan(\dfrac{B}{A}))$

$$\sqrt{A^2+B^2}(\sin(x)\cos(\arctan(\frac{B}{A})) + \cos(x)\sin(\arctan(\frac{B}{A}))) + C = y$$

let $\phi = \arctan(\dfrac{B}{A})$ and $D = \sqrt{A^2+B^2}$

$$D(\sin(x)\cos(\phi) + \cos(x)\sin(\phi)) + C = y$$

where $x = \frac{t}{12}$

$$D\sin(\frac{t}{12} + \phi) + C = y$$

So $A\sin(x) + B\cos(x) + C = y$ is a sine with amplitude $D = \sqrt{A^2+B^2}$ and phase $\phi = \arctan(\dfrac{B}{A})$. This form offers advantages, as A and B can be spatially averaged, whereas averaging ϕ of several gridpoints can lead to unwanted results. For example, when averaging two points in space, one with a phase of November, one with January, the intuitive average would be December. Averaging phases of 15° and 330° (roughly corresponding to January and November) however, yields a phase of 172.5°, which roughly corresponds to July.

II Python Script for Regridding and Calculations

```
#
# this script regrids ORCA U and V grid data to T grid data and
# calulates EKE and tau at the surface, vertical shear and potential
# density, input has to have time dimension length 1!
#
# eight input arguments are needed
# 1: netcdf file containing U and utau
# 2: netcdf file containing V and vtau
# 3: netcdf file containing mean U, to which
#           deviations should be calculated for EKE
# 4: same as 3, but for V
# 5: netcdf file with T,S and the T grid coordinates
# 6: output file name for EKE and tau on horizontal T grid at z=0
# 7: output file name for veritcal shear on horizontal T grid
#           and vertical interpolated grid
# 8: output file name for potential density on horizontal
#           and vertical T grid
#
# import required modules
import numpy as np
from netCDF4 import Dataset as nc
from seawater import csiro as sea
import sys
#
# fetching input arguments
input1=sys.argv[1]
input2=sys.argv[2]
input3=sys.argv[3]
input4=sys.argv[4]
input5=sys.argv[5]
input6=sys.argv[6]
input7=sys.argv[7]
input8=sys.argv[8]
#
# extract variables from netcdf files
uin=nc.netcdf_file(input1,'r')
u=uin.variables['vozocrtx'][:]       # U
utau=uin.variables['vozotaux'][:]    # utau
uin.close()
vin=nc.netcdf_file(input3,'r')
v=vin.variables['vomecrty'][:]       # V
vtau=vin.variables['vometauy'][:]    # vtau
vin.close()
u_in=nc.netcdf_file(input2,'r')
u_=u_in.variables['vozocrtx'][:]     # mean U
u_in.close()
v_in=nc.netcdf_file(input4,'r')
v_=v_in.variables['vomecrty'][:]     # mean V
timein=v_in.variables['time'][:]     # time (could be extracted from
v_in.close()                         # any other input file as well
t=nc.netcdf_file(input5,'r')
nav_latin=t.variables['nav_lat'][:]  # T grid latitude
nav_lonin=t.variables['nav_lon'][:]  # T grid longitude
depthtin=t.variables['deptht'][:]    # T grid depth
temp=t.variables['votemper'][:]      # temperature
sal=t.variables['vosaline'][:]       # salinity
t.close()
#
# depth array, define 3-d depth array with same dimensions as T,S etc
D=np.ma.empty_like(u)
for i in np.arange(0,20):
   D[i,:,:]=depthtin[i]

#
# eke calculation
# first calculate deviations from the mean
udev=u_-u
vdev=v_-v
#
# interpolate u_dev and v_dev to T grid (averaging U(i-1) and U(i)
# gives U at T grid point i etc)
# insert columns of zeros at the end (u_dev1) and beginning (u_dev2)
```

```
# of u_dev to shift u_dev2 by one column, then average u_dev1(i) and
# u_dev2(i).
u_dev1=np.insert(u_dev, np.shape(nav_lat)[1], 0, axis=3)
u_dev2=np.insert(u_dev, 0, 0, axis=3)
#
# the same for v_dev, but here shift one row
v_dev1=np.insert(v_dev, np.shape(nav_lat)[0], 0, axis=2)
v_dev2=np.insert(v_dev, 0, 0, axis=2)
#
# averaging and cutting away first and last rows and columns
# to get rid of spurious grid points
udev_t=0.5*(u_dev1+u_dev2)[:,:,1:np.shape(nav_lat)[0],1:-1]
vdev_t=0.5*(v_dev1+v_dev2)[:,:,1:-1,1:np.shape(nav_lat)[1]]
#
# then calculate eke on the T grid
eke_t=0.5*((udev_t*udev_t)+(vdev_t*vdev_t))
#
# same procedure for the windstress calculation
utau1=np.insert(utau, np.shape(nav_lat)[1], 0, axis=2)
utau2=np.insert(utau, 0, 0, axis=1)
vtau1=np.insert(vtau, np.shape(nav_lat)[0], 0, axis=1)
vtau2=np.insert(vtau, 0, 0, axis=0)
utau_t=0.5*(utau1+utau2)[:,1:np.shape(nav_lat)[0],1:-1]
vtau_t=0.5*(vtau1+vtau2)[:,1:-1,1:np.shape(nav_lat)[1]]
#
# calculating the absolute windstress on the T grid
tau_t=np.ma.sqrt((utau_t*utau_t)+(vtau_t*vtau_t))
#
# calculate potential density with the seawater library
# first define a pressure array
P=sea.pres(D,nav_latin)
potT=sea.ptmp(sal,temp,P,0.) # potential temperature
potD=sea.dens(sal,potT,P)    # potential density
#
# calculate vertical shear
# first regrid to the T grid as before
u1=np.insert(u, np.shape(nav_lat)[1], 0, axis=3)
u2=np.insert(u, 0, 0, axis=3)
v1=np.insert(v, np.shape(nav_lat)[0], 0, axis=2)
v2=np.insert(v, 0, 0, axis=2)
u_t=0.5*(u1+u2)[:,:,1:np.shape(nav_lat)[0],1:-1]
v_t=0.5*(v1+v2)[:,:,1:-1,1:np.shape(nav_lat)[1]]
#
# calculate the speed
vel=np.ma.sqrt((u_t*u_t)+(v_t*v_t))
#
# now doing the regridding for the vertical grid
# because du/dz points lie in between the T grid depth
vel1=np.insert(vel, 0, 0, axis=0)
vel2=np.insert(vel, 46, 0, axis=0)
depth1=np.insert(D, 0, 0, axis=0)
depth2=np.insert(D, 46, 0, axis=0)
d1=np.insert(depthtin, 0, 0, axis=0)
d2=np.insert(depthtin, 46, 0, axis=0)
#
# calculating Du/dz
she=((vel1-vel2)/(depth1*(-1.)-depth2*(-1.)))[1:-1,:,:]
#
# and interpolate the depth vector
shedepth=0.5*(d1+d2)[1:-1]
#
# finally, creating the output variables with the names
# defined in the input arguments
# first, create the netcdf file for eke and tau
out=nc.netcdf_file(input6,'w')
#
# create the dimensions
out.createDimension('deptht',46)
out.createDimension('y',np.shape(udev)[2])
out.createDimension('x',np.shape(udev)[3])
out.createDimension('time',1)
#
```

```
# create variables and then write data to them
deptht=out.createVariable('deptht','d',('deptht',))
deptht[:]=depthtin
nav_lat=out.createVariable('nav_lat','d',('y', 'x',))
nav_lat[:]=nav_latin[1:np.shape(potT)[0],1:np.shape(potT)[1]]
nav_lon=out.createVariable('nav_lon','d',('y', 'x',))
nav_lon[:]=nav_lonin[1:np.shape(potT)[0],1:np.shape(potT)[1]]
time=out.createVariable('time','d',('time',))
time[:]=timein
eke=out.createVariable('eke','d',('time','deptht','y','x',))
eke[:]=eke_t
tau_T=out3.createVariable('tau','d',('time','y','x',))
tau_T[:]=tau_t
out.close()
#
# netcdf file for the vertical shear
out2=nc(input7,'w')
#
# create the dimensions
out2.createDimension('y',np.shape(she)[0])
out2.createDimension('x',np.shape(she)[1])
out2.createDimension('time',1)
out2.createDimension('depthtdz',45)
#
# create variables and then write data to them
depthtdz=out2.createVariable('depthtdz','d',('depthtdz',))
depthtdz[:]=shedepth
nav_lat=out2.createVariable('nav_lat','d',('y', 'x',))
nav_lat[:]=nav_latin[1:np.shape(potT)[0],1:np.shape(potT)[1]]
nav_lon=out2.createVariable('nav_lon','d',('y', 'x',))
nav_lon[:]=nav_lonin[1:np.shape(potT)[0],1:np.shape(potT)[1]]
time=out2.createVariable('time','d',('time',))
time[:]=timein
vertshear=out2.createVariable('vertshear','d',('time','depthtdz','y','x',))
vertshear[:]=she
out2.close()
#
# and the netcdf file for potential temperature and density
out3=nc(input8,'w')
#
# create the dimensions
out3.createDimension('y',np.shape(potT)[0])
out3.createDimension('x',np.shape(potT)[1])
out3.createDimension('time',1)
out3.createDimension('deptht',46)
#
# create variables and then write data to them
deptht=out3.createVariable('deptht','d',('deptht',))
deptht[:]=depthtin
nav_lat=out3.createVariable('nav_lat','d',('y', 'x',))
nav_lat[:]=nav_latin
nav_lon=out3.createVariable('nav_lon','d',('y', 'x',))
nav_lon[:]=nav_lonin
time=out3.createVariable('time','d',('time',))
time[:]=timein
potT_T=out3.createVariable('potT_T','d',('time','deptht','y','x',))
potT_T[:]=potT
potD_T=out3.createVariable('potD_T','d',('time','deptht','y','x',))
potD_T[:]=potD
out.close()
```

Acknowledgements

I thank Claus Böning and Richard Greatbatch for supervision during the writing of this thesis, as well as Markus Scheinert for continuous technical support regarding the ORCA12 model and data analysis/visualization.

Further thanks go to Mia Schumacher, Hanna Schade and Friedrich Bergmann for helpful comments and general support.

Erklärung

Hiermit erkläre ich, dass ich die vorliegende Arbeit selbständig und ohne fremde Hilfe angefertigt und keine anderen als die angegebenen Quellen und Hilfsmittel verwendet habe. Die eingereichte schriftliche Fassung der Arbeit entspricht der auf dem elektronischen Speichermedium.
(Name der Datei: Rieck_817219_Master_Thesis.pdf)
Weiterhin versichere ich, dass diese Arbeit noch nicht als Abschlussarbeit an anderer Stelle vorgelegen hat.

Kiel, 22.10.2014